ELSEVIER

Frictional sliding modes along an interface between identical elastic plates subject to shear impact loading

D. Coker[a], G. Lykotrafitis[b], A. Needleman[a],*, A.J. Rosakis[b]

[a]*Division of Engineering, Brown University, 182 Hope Street, Providence, RI 02912, USA*
[b]*Division of Engineering and Applied Science, California Institute of Technology, Pasadena, CA 91125, USA*

Abstract

Frictional sliding along an interface between two identical isotropic elastic plates under impact shear loading is investigated experimentally and numerically. The plates are held together by a compressive stress and one plate is subject to edge impact near the interface. The experiments exhibit both a crack-like and a pulse-like mode of sliding. Plane stress finite element calculations modeling the experimental configuration are carried out, with the interface characterized by a rate and state dependent frictional law. A variety of sliding modes are obtained in the calculations depending on the impact velocity, the initial compressive stress and the values of interface variables. For low values of the initial compressive stress and impact velocity, sliding occurs in a crack-like mode. For higher values of the initial compressive stress and/or impact velocity, sliding takes place in a pulse-like mode. One pulse-like mode involves well-separated pulses with the pulse amplitude increasing with propagation distance. Another pulse-like mode involves a pulse train of essentially constant amplitude. The propagation speed of the leading pulse (or of the tip of the crack-like sliding region) is near the longitudinal wave speed and never less than $\sqrt{2}$ times the shear wave speed. Supersonic

---

*Corresponding author. Tel.: +14018632863; fax: +14018639009.
E-mail address: needle@brown.edu (A. Needleman).

trailing pulses are seen both experimentally and computationally. The trends in the calculations are compared with those seen in the experiments.

1. Introduction

Frictional sliding along an interface between two rapidly deforming solids is a basic problem of mechanics that arises in a variety of contexts including moving machinery surface interaction (both macro and micro machines), material processing (e.g. cutting), the failure of fiber reinforced composites (e.g. fiber pullout) and earthquake dynamics (fault rupture). However, a framework for quantifying the wide range of observed dynamic frictional phenomena is only beginning to emerge. The classical Amontons–Coulomb description of friction states that the shear stress at an interface is proportional to the normal stress, with the coefficient of proportionality being the coefficient of friction. Two coefficients of friction are identified; a static coefficient of friction that governs the onset of sliding and a dynamic coefficient of friction that characterizes the behavior during sliding.

At the microscale, an evolving population of deforming and fracturing contacts, possible phase transitions and the presence of various lubricants play an important role in setting the static and dynamic coefficients of friction as well as in governing the transition between them. Rate and state models of friction aim at incorporating the effects of these microscale processes through appropriately chosen state variables, e.g. Dieterich (1979), Ruina (1983), Rice and Ruina (1983), Linker and Dieterich (1992), Prakash and Clifton (1993), and Prakash (1998).

Rate and state models of friction have come to the fore because they substantially influence the predicted mode and stability of sliding. Of particular interest is whether sliding occurs in a crack-like mode in which the surfaces behind the leading edge of sliding continuously slide or in a pulse-like mode, first proposed by Heaton (1990), in which sliding occurs over a relatively small propagating region. One significance of the sliding mode is that the calculated frictional dissipation in the pulse-like mode is significantly less than in the crack-like mode and is consistent with some values of heat generation inferred from geophysical field measurements (Heaton, 1990).

The classical Amontons–Coulomb description of friction is inadequate for addressing fundamental issues of sliding along interfaces between elastic solids because with Amontons–Coulomb friction sliding along such an interface is unstable to periodic perturbations for a wide range of friction coefficients and material properties, with a growth rate proportional to the wave number (Renardy, 1992; Adams, 1995). When generalized Rayleigh waves exist, Ranjith and Rice (2001) found that there are unstable modes for all values of the friction coefficient. Mathematically, instability of periodic perturbations renders the response of a material interface with Amontons–Coulomb friction ill-posed. Physically, it implies that during sliding energy is transferred to shorter wave lengths, leading to pulse

sharpening and splitting. Numerically, the splitting of individual pulses creates an inherent grid-size dependence (Andrews and Ben-Zion, 1997; Ben-Zion and Andrews, 1998). Ranjith and Rice (2001) showed that an experimentally based rate and state dependent friction law (Prakash and Clifton, 1993; Prakash, 1998), in which the shear strength in response to an abrupt change in normal stress evolves continuously with time, regularizes the problem. Convergence through grid size reduction is then achieved (Cochard and Rice, 2000).

Although rate- and state-dependent frictional laws provide regularization, slip pulses may still grow with time. Perrin et al. (1995) and Zheng and Rice (1998) found from anti-plane strain (mode-III) calculations conditions on the frictional law and the loading conditions needed for well-posedness. They also found that under certain conditions, which include the rate of steady state velocity weakening, sliding can be partially crack-like and partially pulse-like. Ben-Zion and Huang (2002) numerically analyzed a configuration of two identical solids separated by a variable-width fault zone layer and assumed constant external compressive and shear fields. They showed that the friction law used by Ranjith and Rice (2001) and Cochard and Rice (2000) regularizes the Adams instability for identical as well as for dissimilar materials. The same conclusion was reached analytically by Rice et al. (2001). The use of rate and state dependent friction not only regularizes the ill-posedness of the sliding problem but can also eliminate supersonic propagation (Rice et al., 2001). However, the physical reason for excluding supersonic propagation is not clear.

The issue of limiting propagation speeds arises in the dynamic fracture mechanics of growing shear cracks (Freund, 1998; Broberg, 1999; Rosakis, 2002) which has many similarities with the frictional sliding process. Early analytical and numerical studies of intersonic shear crack growth using continuum slip weakening (Burridge, 1973), 1973; Andrews, 1976; Broberg, 1995, 1996) and velocity weakening cohesive zone models (Samudrala et al., 2002) concentrated on elucidating the mechanism of transition from sub-Rayleigh to super-shear wave propagation speeds, see also Madariaga and Olsen (2000) and Dunham et al. (2003), and on the identification of stable intersonic propagation speed regimes. Of particular relevance to the present study is the persistent occurrence of intersonic shear rupture along interfaces between identical solids which was first observed experimentally by Rosakis et al. (1999) and by Coker and Rosakis (2001). This phenomenon was subsequently modeled numerically by Needleman (1999) and by Hao et al. (2004). Atomistic models of intersonic shear rupture (Abraham and Gao, 2000; Abraham, 2001; Gao et al., 2001), field observations of intersonic rupture events during recent large crustal earthquakes (Archuleta, 1984; Olsen et al., 1997; Hernandez et al., 1999; Bouchon et al., 2001; Lin et al., 2002; Bouchon and Vallee, 2003), as well as recent laboratory models of earthquake rupture (Xia et al., 2004) have demonstrated the remarkable length scale persistence (over eleven orders of magnitude) of intersonic rupture phenomena and of the main features observed in laboratory experiments and in continuum theories.

Here, frictional sliding between identical rectangular plates subject to an initial compressive stress and impact shear loading is studied both experimentally and numerically. In the experiments, a uniform compressive stress is applied to two

Homalite plates and the impact loading is imposed using a gas gun and a steel projectile. Dynamic photoelasticity is used to record fringe patterns on a microsecond time-scale. The fringe patterns give indirect evidence of the sliding mode and the propagation speed of the sliding tip is measured. Plane stress calculations modeling the experimental configuration are carried out with friction characterized by a rate- and state-dependent relation, including the Prakash–Clifton (Prakash and Clifton, 1993; Prakash, 1998) normal stress dependence. A parameter study is undertaken to predict possible modes of sliding in this configuration together with the associated propagation speeds. The dependence on loading conditions is explored and the computational results are compared with the experimental observations.

2. Formulation

2.1. Boundary value problem

We consider two solids undergoing relative motion across an interface S_{int}. A framework is used where two constitutive relations are specified; one for the plate material and one to characterize frictional sliding in terms of the traction and velocity jump across the interface. Plane stress conditions are assumed, geometry changes are neglected[1] and the principle of virtual work is written as

$$\int_A \boldsymbol{\sigma} : \delta\boldsymbol{\varepsilon}\,dA - \int_{S_{\text{int}}} \mathbf{T} \cdot \delta\Delta\mathbf{u}\,dS = \int_{S_{\text{ext}}} \mathbf{T} \cdot \delta\mathbf{u}\,dS - \int_A \rho\frac{\partial^2 \mathbf{u}}{\partial t^2} \cdot \delta\mathbf{u}\,dA, \tag{1}$$

where t is time, $\boldsymbol{\sigma}$ is the stress tensor, $\boldsymbol{\varepsilon}$ is the strain tensor, $\mathbf{u}$ is the displacement vector, $\mathbf{T}$ is the traction vector, $\Delta\mathbf{u}$ is the displacement jump across the interface, $\boldsymbol{\sigma} : \boldsymbol{\varepsilon}$ denotes $\sigma_{ij}\varepsilon_{ji}$, and A, S_{ext} and S_{int} are the area, external boundary, and interface line, respectively, in the reference configuration.

Computations are carried out for the specimen geometry shown in Fig. 1 with $\ell = 75\,\text{mm}$ and $w = 132\,\text{mm}$. A Cartesian coordinate system with the $x_1 - x_2-$ plane being the plane of deformation is used and the origin is taken as shown in Fig. 1. The plates are subject to a uniform compressive stress of magnitude Σ_0. For $t \leqslant 0$, $S_{22} = -\Sigma_0$ and $T_{\text{n}} = \Sigma_0$ along the interface. Displacements are measured from the uniformly compressed state at $t = 0^-$.

At $t = 0^+$, a normal velocity is prescribed along the portion of the edge $x_1 = 0$ for which $-b \leqslant x_2 \leqslant 0$, with $b = 25\,\text{mm}$, and the shear traction is taken to vanish there. Hence,

$$u_1 = -\int_0^t V(\xi)\,d\xi, \quad T_2 = 0, \quad \text{on } x_1 = 0 \quad \text{and} \quad -b \leqslant x_2 \leqslant 0, \tag{2}$$

---

[1]The calculations are carried out using a finite element code developed for finite deformations in which the constitutive relation is expressed in terms of second Piola–Kirchhoff stress and Lagrangian strain components; otherwise finite deformation effects are neglected in the calculations here.
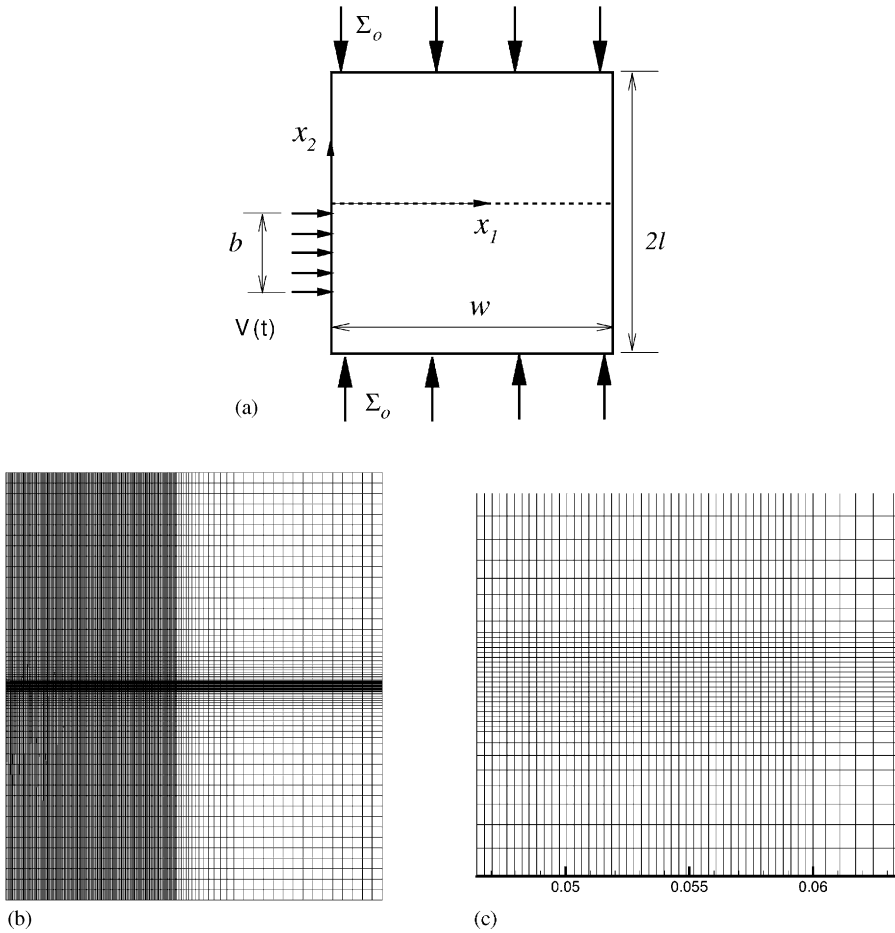
(a)

(b)

(c)

Fig. 1. (a) Geometry and loading configuration used in the plane stress finite element calculations. (b) The finite element mesh used in the calculations (56,580 degrees of freedom). (c) Close up of the mesh near the transition along the x_1 axis between the uniform and graduated mesh regions; distances are in *m*.

where in Eq. (2)

$$V(t) = \begin{cases} V_{\text{imp}}\, t/t_{\text{r}}, & \text{for } 0 \leqslant t < t_{\text{r}}, \\ V_{\text{imp}}, & \text{for } t_{\text{r}} \leqslant t \leqslant t_{\text{p}}, \\ V_{\text{imp}}\,[1 - (t - t_{\text{p}})/t_{\text{s}}], & \text{for } t_{\text{p}} < t < (t_{\text{p}} + t_{\text{s}}), \\ 0, & \text{for } t \geqslant (t_{\text{p}} + t_{\text{s}}). \end{cases} \tag{3}$$

Here, t_{r} is the rise time, t_{p} is the pulse time and t_{s} is the step down time. In the calculations t_{r} and t_{s} are fixed at $10\,\mu\text{s}$ and $(t_{\text{p}} - t_{\text{r}})$ is $50\,\mu\text{s}$. On the remaining external surfaces of the specimen $\mathbf{T} = \mathbf{0}$.

The plate material is characterized as an isotropic elastic solid with Young's modulus E and Poisson's ratio v. In plane stress, the longitudinal, c_l, shear, c_s, and Rayleigh, c_R, wave speeds are given by

$$c_l = \sqrt{\frac{E}{\rho(1 - v^2)}}, \quad c_s = \sqrt{\frac{E}{2\rho(1 + v)}}, \quad c_R = c_s \frac{0.86 + 1.14v}{1 + v}. \tag{4}$$

Using elastic properties representative of Homalite-100: $E = 5.3\,\text{GPa}$, $v = 0.35$ and density $\rho = 1246\,\text{kg/m}^3$, the elastic wave speeds in Eq. (4) are given by

$$c_l = 2201\,\text{m/s}, \quad c_s = 1255\,\text{m/s}, \quad c_R = 1170\,\text{m/s}. \tag{5}$$

A rate- and state-dependent friction law is taken to characterize the response along the interface $x_2 = 0$. With n and s, respectively, denoting in-plane directions normal and tangential to the interface, $\Delta \dot{u}_n$ and $\Delta \dot{u}_s$ are the difference in velocity between material points that are on opposite sides of the interface in the initial configuration. Since the change in the positions of material points along the interface is not accounted for, the formulation is restricted to small amounts of sliding. When $\Delta u_n > -\Sigma_0/C_n$, the interface is in tension and

$$T_n = 0, \quad T_s = 0, \tag{6}$$

along S_{int}. Otherwise,

$$\dot{T}_n = -C_n \Delta \dot{u}_n, \tag{7}$$

$$\dot{T}_s = C_s[\Delta \dot{u}_s - \text{sgn}(T_s)\Delta \dot{u}_{\text{slip}}]. \tag{8}$$

Here, as in Povirk and Needleman (1993), the interface is presumed to have an elastic stiffness and $\Delta \dot{u}_{\text{slip}}$ is the magnitude of the sliding velocity specified by the rate- and state-dependent friction law ($\Delta \dot{u}_{\text{slip}} \geqslant 0$). In the elastic-friction relation Eq. (8) $\Delta \dot{u}_{\text{slip}}$ is an internal variable determined from the frictional constitutive description, while $\Delta \dot{u}_s$ is the jump in particle velocity across the interface. Unless otherwise specified, the values $C_n = 300\,\text{GPa/m}$ and $C_s = 100\,\text{GPa/m}$ are used in the calculations here. These values give good agreement with the observed behavior of the head wave under symmetric loading conditions as noted in Section 4.1.

The finite element discretization is based on linear displacement triangular elements that are arranged in a 'crossed-triangle' quadrilateral pattern. When the finite element discretization of the displacement field is substituted into Eq. (1) and the integrations are carried out, equations of the form

$$\mathbf{M} \frac{\partial^2 \mathbf{U}}{\partial t^2} = \mathbf{R}, \tag{9}$$

are obtained where $\mathbf{U}$ is the vector of nodal displacements, $\mathbf{M}$ is the mass matrix and $\mathbf{R}$ is the nodal force vector consisting of contributions from the area elements and the interface. Four point Gaussian integration is used along the interface. The governing equations are integrated using a central difference scheme that can be regarded as a member of the Newmark β family of time integration algorithms, Belytschko et al. (1976). A lumped mass matrix is used instead of the consistent mass matrix, since this

has been found preferable for explicit time integration procedures, from the point of view of accuracy as well as computational efficiency (Krieg and Key, 1973).

The mesh used in the calculations consists of a fine region with uniform rectangular elements near the interface at impact edge, with the mesh spacing then gradually increasing in size. The mesh has 18,320 quadrilateral elements and 56,580 degrees of freedom, with the uniform mesh region consisting of 200×20 rectangles, each of which is 0.30 mm $\times$ 0.20 mm, so that the uniform mesh extends 60 mm from the impact edge. The configuration analyzed and the finite element mesh used are shown in Fig. 1.

2.2. Rate- and state-dependent friction law

The classical Amontons–Coulomb frictional relation has the form

$$|T_s| = \mu T_n, \tag{10}$$

where T_n is the component of $\mathbf{T}$ in the direction of the normal to the interface, T_s is the component of $\mathbf{T}$ tangent to the sliding direction and μ is the (constant) coefficient of friction. The relation (10) holds when the normal traction is compressive, i.e. with the sign convention here when $T_n > 0$.

The problem of two elastic half-spaces sliding with a constant coefficient of friction, μ, is ill-posed for a significant range of values of μ, Adams (1995). This manifests itself in numerical solutions through a lack of convergence with increasing mesh refinement. Rate and state dependent friction laws were introduced, mainly in the geophysics literature, to account for experimental observations that could not be rationalized in the context of a Coulomb friction description. At each point on the interface, the coefficient of friction μ in Eq. (10) is taken to depend on the frictional sliding velocity at that point, $\Delta \dot{u}_{slip}$, and a set of state variables, θ_i so that

$$|T_s| = \mu(\theta_i, \Delta \dot{u}_{slip}) T_n.$$

The state variables are regarded as phenomenological parameters that account for the change of contact quality between the surfaces over time. Rate and state dependent friction models can account for the following fundamental observations on friction (Dieterich, 1979, Rice and Ruina, 1983; Ruina, 1983):

 (i) There is an instantaneous increase in the coefficient of friction in response to a step increase $\Delta \dot{u}_{slip}$ (the direct effect),
 (ii) there is a subsequent change to a steady-state value of the coefficient of friction with this steady-state value being a decreasing function of $\Delta \dot{u}_{slip}$, and
(iii) the approach to this steady-state value occurs over a characteristic distance that is independent of $\Delta \dot{u}_{slip}$.

Another key observation is that transmitted shear stresses do not instantaneously follow a step drop in the normal stresses, Prakash and Clifton (1993), Prakash (1998). Instead, immediately following a step drop in $|T_n|$, as the slip accumulates the shear stress gradually approaches a new steady-state level characteristic of the

new normal pressure and the current sliding velocity, Prakash and Clifton (1993). The relation, Eq. (10), is replaced by, Prakash and Clifton (1993), Prakash (1998),

$$|T_s| = \mu(\theta_0, \Delta\dot{u}_{slip})(\theta_1 + \theta_2), \tag{11}$$

with the evolution of the state variables θ_1 and θ_2 given by

$$\dot{\theta}_1 = -\frac{1}{L_1}[\theta_1 - CT_n]\Delta\dot{u}_{slip}, \tag{12}$$

$$\dot{\theta}_2 = -\frac{1}{L_2}[\theta_2 - DT_n]\Delta\dot{u}_{slip}, \tag{13}$$

where L_1 and L_2 are characteristic lengths. In the steady state, when $\dot{\theta}_1 = 0$ and $\dot{\theta}_2 = 0$, Eqs. (11)–(13) imply $T_s \propto T_n$.

In Dieterich (1979); Rice and Ruina (1983) and Ruina (1983) μ was taken to have a logarithmic dependence on the sliding velocity. In such a relation, μ is not bounded at $\Delta\dot{u}_{slip} = 0$ which leads to difficulties in numerical computations. Rice and Ben-Zion (1996) and Ben-Zion and Rice (1997) appealed to an activated rate process interpretation which resulted in a relation bounded at $\Delta\dot{u}_{slip} = 0$. Here, we adopt a purely phenomenological expression for μ proposed by Povirk and Needleman (1993) that has the form

$$\mu(\theta_0, \Delta\dot{u}_{slip}) = g(\theta_0)\left(\frac{\Delta\dot{u}_{slip}}{V_0} + 1\right)^{1/m}, \tag{14}$$

with

$$g(\theta_0) = \frac{\mu_d + (\mu_s - \mu_d)\exp\left[-\left(\frac{L_0/\theta_0}{V_1}\right)^p\right]}{\left[\frac{L_0/\theta_0}{V_0} + 1\right]^{1/m}}, \tag{15}$$

where the evolution of θ_0 is given by,

$$\dot{\theta}_0 = B\left(1 - \frac{\theta_0 \Delta\dot{u}_{slip}}{L_0}\right) \tag{16}$$

and μ_s, μ_d, L_0, V_0, V_1 and B are prescribed constants. We note that the internal variable θ_0 has the dimension of time, while the internal variables θ_1 and θ_2 have the dimension of stress.

The steady-state value of θ_0, i.e. the value at which $\dot{\theta}_0 = 0$ is $L_0/\Delta\dot{u}_{slip}$. Substituting this value into Eqs. (14) and (15) gives the steady-state value for the friction coefficient, μ_{ss}, at sliding velocity $\Delta\dot{u}_{slip}$ as

$$\mu_{ss} = \mu_d + (\mu_s - \mu_d)\exp\left[-\left(\frac{\Delta\dot{u}_{slip}}{V_1}\right)^p\right]. \tag{17}$$

The frictional relation Eq. (8) is only invoked if there is contact ($T_n \geqslant 0$). Even when there is contact, $\Delta \dot{u}_{\text{slip}}$ may still vanish. Define

$$\beta = \frac{|T_s|}{g(\theta_0)(\theta_1 + \theta_2)}, \tag{18}$$

then from Eqs. (11) and (14), and requiring $\Delta \dot{u}_{\text{slip}}$ to be non-negative, $\Delta \dot{u}_{\text{slip}}$ is given by

$$\Delta \dot{u}_{\text{slip}} = \begin{cases} V_0(\beta^m - 1), & \text{for } \beta > 1, \\ 0, & \text{for } \beta \leqslant 1. \end{cases} \tag{19}$$

Note that $\beta > 1$ implies $|T_s| - g(\theta_0)(\theta_1 + \theta_2) > 0$. When the normal traction is constant $\theta_1 + \theta_2 = T_n$ and β simplifies to $|T_s|/T_n g(\theta_0)$ as in Povirk and Needleman (1993).

We refer to circumstances where $\Delta \dot{u}_{\text{slip}} = 0$ as sticking and circumstances where $\Delta \dot{u}_{\text{slip}} > 0$ as frictional sliding.

The procedure used to carry out time integration of this frictional constitutive relation is described in the appendix.

2.3. Friction law parameters

Samudrala et al. (2002) and Rosakis (2002) fit sliding experiments of Homalite on Homalite (Rosakis et al., 1999, 2000) with an expression of the form

$$\mu_{ss} = \mu_0 \left[1 + \alpha \frac{\Delta \dot{u}_{\text{slip}}}{c_s} \frac{G}{2\tau_0} \right], \tag{20}$$

where $2G = E/(1 + v)$ and τ_0 is the shear strength of Homalite. From the observed inclination of tensile micro-cracks emanating from the interface, the parameter values $\alpha = -0.4$, $G/\tau_0 = 136$, and $\mu_0 = 0.6$ were obtained.

Parameter values in Eq. (17) were chosen to match the response in Eq. (20) for $\Delta \dot{u}_{\text{slip}} < 40 \, \text{m/s}$. Fig. 2a shows μ_{ss} as a function of $\Delta \dot{u}_{\text{slip}}$ from Eq. (20) and from Eq. (17) with $\mu_s = 0.6$, $\mu_d = 0.5$, $p = 1.2$ and $V_1 = 26 \, \text{m/s}$. The parameters V_0 and m in Eq. (14) were chosen to be consistent with the observed response for $\Delta \dot{u}_{\text{slip}}$ ranging from 10 to 40 m/s (Fig. 2a). Fig. 2b shows the friction coefficient, T_s/T_n, as a function of the accumulated frictional sliding $\Delta u_{\text{slip}} = \int \Delta \dot{u}_{\text{slip}} \, dt$. There is an instantaneous increase in T_s/T_n in the same direction as the change in $\Delta \dot{u}_{\text{slip}}$ (the direct effect) followed by a gradual decrease to a steady-state value. The apparent coefficient of friction T_s/T_n can attain values outside the range defined by the static and dynamic coefficients of friction due to the direct effect in the rate- and state-dependent friction law.

The parameter values for the normal stress dependent response, C, D, L_1, are chosen close to values obtained in the experiments of Prakash and Clifton (1993). The initial values for the internal variables were set to $\theta_0(0) = L/10 \dot{V}_1$ and $\theta_1(0) = C\Sigma_0$ and $\theta_2(0) = D\Sigma_0$. Fig. 3 shows the response using Eqs. (11)–(16) under a step jump in compressive normal traction at a constant sliding velocity. The plots show
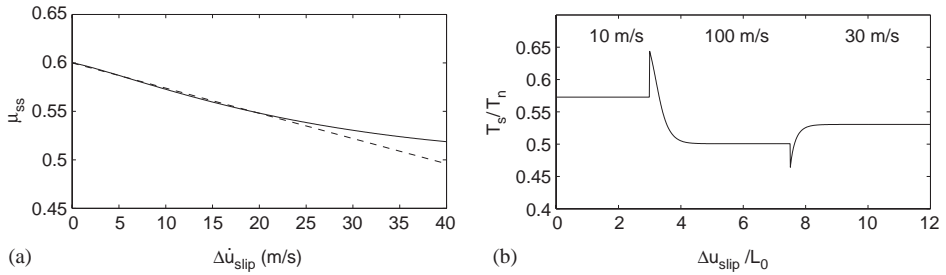
Fig. 2. (a) The steady-state coefficient of friction, μ_{ss}, as a function of $\Delta\dot{u}_{slip}$ for Eq. (20) (dashed line) and for Eq. (17) using the properties in Table 1 (solid line). (b) The effect of an abrupt change in $\Delta\dot{u}_{slip}$ on the apparent coefficient of friction T_s/T_n for the rate- and state-dependent friction relation used in the calculations.
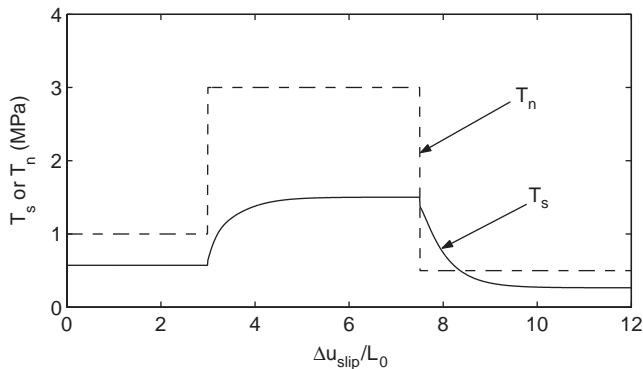

Fig. 3. Variation of the shear traction, T_s, (solid line) as a function of Δu_{slip} for a step jump in compressive normal traction, T_n, (dashed line) at constant frictional sliding rate $\Delta\dot{u}_{slip}$ for the rate- and state-dependent friction relation used in the calculations.

the imposed normal traction (dashed line) and the shear traction (solid line) as functions of the accumulated frictional sliding Δu_{slip}. There is a gradual change of the state variables and the shear resistance after a step decrease in the normal compressive stress. The apparent coefficient of friction, T_s/T_n, however, has a sudden jump.

The choice of the initial values for the state variables is arbitrary but can be of significance when comparing to other friction models such as slip-weakening models (Bizzarri et al., 2001). The parameters characterizing the frictional constitutive relation used in the calculations are those in Table 1 unless specifically stated otherwise.

3. Experimental methods and results

The experimental procedures are similar to those used to study shear crack propagation (Rosakis et al., 1999). Two Homalite plates, each with $\ell = 76.2\,\text{mm}$

Table 1
Friction parameter values used in the finite element calculations

Property	Value
μ_s	0.6
μ_d	0.5
V_0 (m/s)	100
V_1 (m/s)	26
B	4.60
p	1.2
m	5
L_0 (m)	20×10^{-6}
L_1 (m)	20×10^{-6}
L_2 (m)	20×10^{-6}
C	0.7
D	0.3

$w = 139.7$ mm (see Fig. 1a) and 9.525 mm thick are held together by a uniform compressive stress. Homalite is a brittle polyester resin that exhibits stress induced birefringence and is mildly rate sensitive. At a strain rate of $10^3 \, \text{s}^{-1}$ the elastic wave speeds are given by Eq. (5). The impact loading is imposed via a cylindrical steel projectile of diameter 25 mm and length 51 mm fired using a gas gun with impact speeds ranging from 10 to 60 m/s. A steel buffer plate, 25.4 mm × 76.2 mm and 9.525 mm thick, is bonded to the impacted plate to prevent shattering at the impact side ($x_1 = 0$ in Fig. 1a) and to induce a more or less planar loading wave. A uniform compressive stress is applied by a press which was calibrated using a load cell. The loading wave, as measured from a strain gage glued to the specimen, is of a trapezoidal form with a rise time of 10–20 μs followed by an essentially steady velocity for 40 μs. Dynamic photoelasticity is used to extract stress field information around the interface. The photoelastic fringe patterns were recorded in real time using a high-speed Cordin CCD camera capable of capturing 16 images at a rate of 100 million frames per second. A collimated laser beam with a diameter of 130 mm is used to illuminate the specimen. Two pairs of circular polarizer plates, placed on either side of the specimen as described by Rosakis et al. (1999), produce isochromatic fringes. The photoelastic optical setup is arranged for light field.

The isochromatic fringes are related to contours of $\sigma_1 - \sigma_2$, with σ_1 being the maximum in-plane principal stress and σ_2 the minimum in-plane principal stress, through the stress optical relation

$$\sigma_1 - \sigma_2 = \frac{NF_\sigma}{h}, \tag{21}$$

where F_σ is the stress optical coefficient of Homalite, h is the specimen thickness, and N is the isochromatic fringe order.

The experimental results are presented in detail in Lykotrafitis et al. (2005). Here, a few experimental results that illustrate characteristic features are presented for comparison with the numerical calculations.
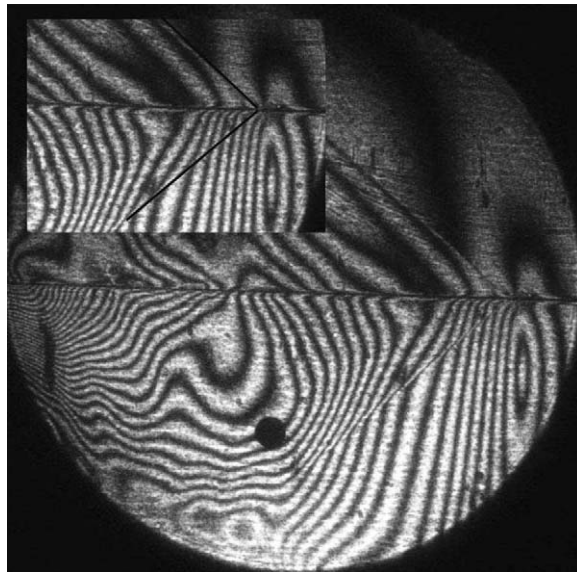
Fig. 4. Experimental isochromatic fringe patterns from a dynamic friction experiment on homalite subject to a static compressive stress of 9.4 MPa and an impact velocity of 32.7 m/s. In the inset lines are drawn to highlight Mach lines. The field of view is 130 mm in diameter.

Results with a compressive stress of 9.4 MPa and impact velocities of 32.7 and 42.2 m/s are presented. Fig. 4 shows the isochromatic fringe patterns obtained with an impact velocity of 32.7 m/s. Experiments conducted at lower impact velocities exhibit similar characteristics. In Fig. 4, the loading wave front, which travels at c_l, arrives from the left. Behind the loading wave front a shear Mach cone, formed by a sharp change in fringe density is observed. The inset to Fig. 4 focuses on the region near the propagating tip with a thick line drawn over the Mach line. The sliding tip follows the loading wave and the tip can be located by tracing the Mach line to the interface. In this case the sliding tip follows shortly behind the dilational loading wave. The propagation speed of the sliding tip is ≈ 1810 m/s as measured by two methods. One measurement involves following the position of the sliding tip in various frames and knowing the frame timing, the propagation speed is obtained. In the second method the Mach angle is used to obtain the tip speed. The two methods give consistent propagation speeds.

In Fig. 4, there is a concentration of isochromatic fringes some distance behind the sliding tip that propagates at approximately c_R and that is a consequence of waves emanating from the projectile corners. Other characteristic features in Fig. 4 are: (i) there is a cusp in the stress contours at the interfaces, indicating that the propagation speed is slightly faster along the interface than in the bulk; (ii) the fringe density is higher in the plate where the impact loading is applied, showing that energy is not transferred easily through the interface; and (iii) the fringe discontinuity at the interface shows that sliding is occurring in a crack-like mode.
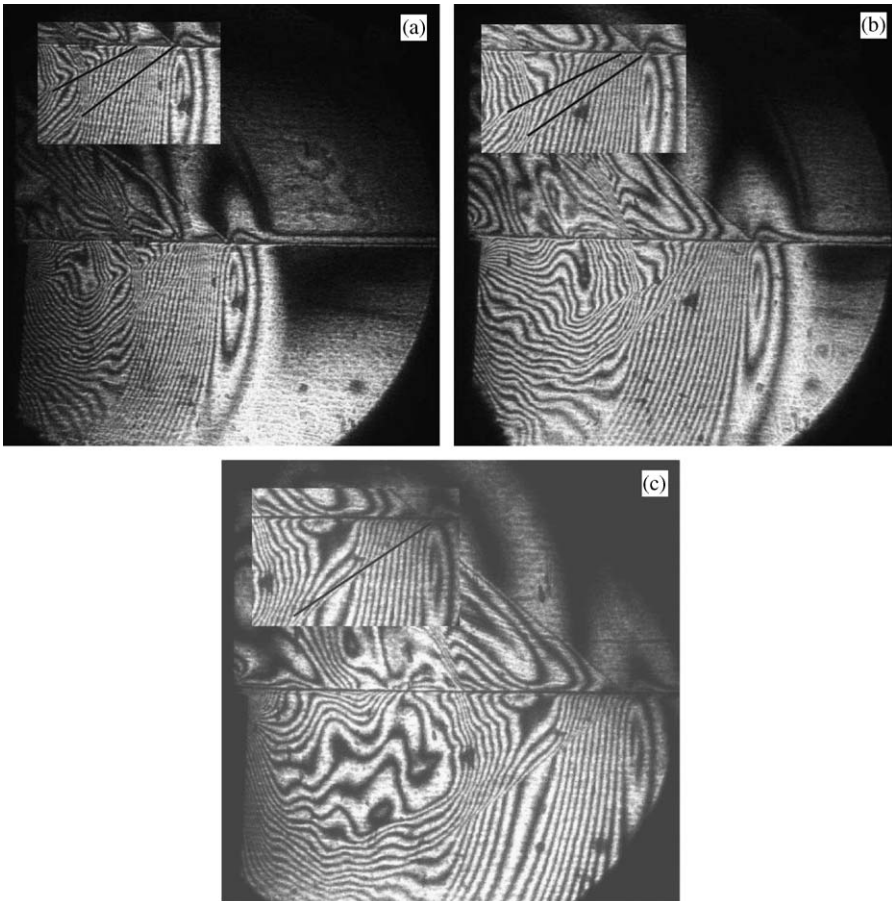
Fig. 5. Experimental isochromatic fringe patterns from a dynamic friction experiment on homalite subject to a static compressive stress of 9.4 MPa and impact velocity of 42 m/s, at (a) $t = 40\,\mu s$, (b) $t = 48\,\mu s$, (c) $t = 60\,\mu s$. In the inset one or more lines are drawn to highlight Mach lines. The field of view is 130 mm in diameter.

Isochromatic fringe patterns for an experiment with an impact velocity of 42 m/s are shown in Fig. 5 at 40, 48 and 60 μs after impact. The thick lines in the insets are drawn to show the Mach line locations and orientations. Both methods of calculating the propagation speed of the sliding tip give a propagation speed of about 1950 m/s. Although the general characteristics seen in Fig. 4 are preserved, new features enrich the picture. Behind the impact wave a shear Mach line emanating from the sliding tip is observed. In addition, a second Mach line emanates behind the sliding tip that is not parallel to the first one (Fig. 5a). This Mach line is at a shallower slope corresponding to a propagation speed of ≈ 2600 m/s which is supersonic with respect to the plane stress longitudinal wave speed. In Fig. 5b the tip of the second Mach line approaches the tip of the first Mach line at the interface.

These two points merge as the second point catches up with the first point (Fig. 5c) and only one Mach line continues to be observed in subsequent frames (not shown).

Behind the second Mach line there is a fringe concentration, associated with the loading, that travels at the Rayleigh wave speed. Some fringes pass continuously from the upper plate to the lower plate which is consistent with a contact region forming. In experiments with the magnitude of the initial compressive stress increased, there is an increase in the number of discontinuous regions of fringe concentration that may indicate separate regions of sliding and regions of sticking (i.e. multiple pulses). In each experiment, the speed of the leading sliding tip is found to be essentially constant. In addition, the propagation speed of the leading sliding tip was found to increase with increasing impact speed (or decreasing compressive stress) and in all cases to be between $\sqrt{2}c_s$ and c_l.

4. Numerical results

The focus here is on illustrating the range of behaviors that are obtained by varying the magnitude of the initial compressive stress Σ_0 and the impact velocity V_{imp}. Results are presented for combinations of Σ_0 and V_{imp} that give rise to the following five sliding modes:

Case I: A crack-like mode—$\Sigma_0 = 6$ MPa, $V_{imp} = 2$ m/s.
Case II: A pulse-like mode—$\Sigma_0 = 30$ MPa, $V_{imp} = 2$ m/s.
Case III: A train of pulses—$\Sigma_0 = 10$ MPa, $V_{imp} = 20$ m/s.
Case IV: Multiple pulses coalescing to form a crack—$\Sigma_0 = 0.9$ MPa, $V_{imp} = 10$ m/s.
Case V: A pulse-like mode followed by a crack-like mode—$\Sigma_0 = 40$ MPa, $V_{imp} = 2$ m/s.

In all cases but Case V, the friction parameters are as specified in Table 1. For Case V, the exponent p in Eq. (15) is taken to be 0.5 and $V_1 = 1$ m/s. Also, for Case IV the values of the interface elastic constants are $C_n = 30$ GPa/m and $C_s = 10$ GPa/m, one tenth their value in all the other cases. In the results presented here, the frictional sliding region remains within the fine uniform part of the mesh.

Results are presented for: (i) propagation speeds; (ii) the spatial distribution and time evolution of various interface quantities; and (iii) isochromatic fringe patterns (contours of $\sigma_1 - \sigma_2$ with σ_1 being the maximum in-plane principal stress and σ_2 the minimum in-plane principal stress).

Curves of propagation speed versus time for all five cases analyzed are shown in Fig. 6. For reference, the longitudinal, c_l, shear, c_s, and $\sqrt{2}c_s$ ($= 1775$ m/s) wave speeds are marked. Also shown in the figure are data points corresponding to measured propagation speeds for the experiment with $\Sigma_0 = 9.4$ MPa and an impact velocity of 42 m/s. The first step in computing the propagation speeds is to record the location of the point furthest from the impact edge where $\Delta\dot{u}_{slip} > 0$. This gives the position of the leading sliding tip at various times and the propagation speed, V_{tip}, is then calculated from this data by a progressive least squares fit using five points. At
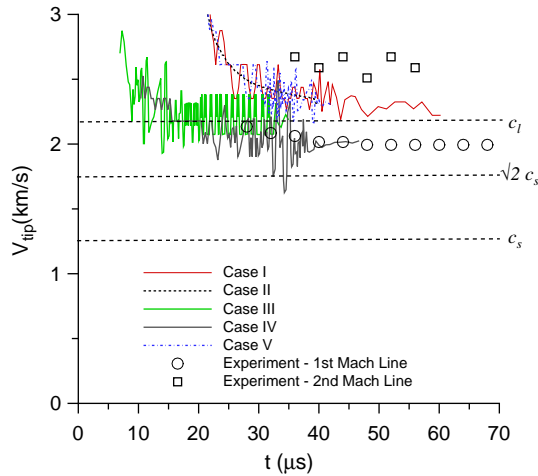
Fig. 6. Propagation speeds, V_{tip}, versus time for the five cases analyzed. The symbols are the experimentally measured propagation speeds from the Mach cone angle with $\Sigma_0 = 9.4$ MPa and $V_{imp} = 42$ m/s (Fig. 5).

least some of the oscillations in propagation speed in Fig. 6 may be due to this numerical differentiation procedure.

Sliding generally initiates somewhat away from the impact edge and then occurs over several small sliding regions that link up. Thus, the process of sliding initiation is not one of propagation of a sliding region but involves jumps in the location of the leading sliding edge. As a consequence, the 'speeds' calculated during the early stages of sliding are unphysically high. Subsequently, the propagation speeds decrease and for Cases II and V, the mean V_{tip} is about c_l whereas for Case IV, after the initial stages of sliding, V_{tip} reduces to ≈ 2000 m/s, in good agreement with the experimental value of 1950 m/s. There are multiple pulses in Case IV and the tip of the second pulse travels at about 2700 m/s, as compared with ≈ 2600 m/s in the experiments. It is worth emphasizing that both the experiments and the calculations indicate that the second pulse travels at a supersonic speed (supersonic with respect to the plane stress longitudinal wave speed). However, for the calculation of Case IV, $\Sigma_0 = 0.9$ MPa and $V_{imp} = 10$ m/s as compared with 9.4 MPa and 42 m/s in the experiments. Hence, there is consistency of propagation speeds for this mode of interface sliding although the loading conditions to achieve this are quite different in the calculations and in the experiments. One possibility for this discrepancy is that the effect of the impedance mismatch between the steel plate bonded to the specimen and Homalite is not accounted for in the computations.

In the following, distributions are shown both for the evolution of $\Delta\dot{u}_s$, which is the particle velocity jump, and for $\Delta\dot{u}_{slip}$, which is the sliding rate obtained from the frictional constitutive relation. From Eq. (8), the difference between these is the 'elastic' sliding rate $\dot{T}_s/C_s$. There are cases where $\Delta\dot{u}_s \approx \Delta\dot{u}_{slip}$ with the elastic sliding

rate being negligible. However, in other cases the difference between $\Delta \dot{u}_s$ and $\Delta \dot{u}_{slip}$ is substantial and the elasticity of the interface then plays a significant role.

The principal stress contours that evolve are a consequence of both the imposed loading and sliding along the interface. To provide a perspective on the contribution of interfacial sliding, the contours of $\sigma_1 - \sigma_2$ that emerge from impact loading with no sliding are considered first.

4.1. Symmetric loading with respect to the interface

In order to illustrate the isochromatic fringe patterns that result without sliding, the symmetric loading configuration shown in the inset of Fig. 7a is analyzed. Fig. 7a shows the simulated isochromatic fringe pattern at $t = 16\,\mu s$ for a calculation carried out with $\Sigma_0 = 10\,\text{MPa}$ and $V_{imp} = 5\,\text{m/s}$. At this time, the loading wave front has propagated 34 mm into the specimen. The isochromatic fringe pattern for a symmetric loading experiment with $\Sigma_0 = 0\,\text{MPa}$ and $V_{imp} = 58\,\text{m/s}$ is shown in Fig. 7b. In both the experiments and simulations the continuity of fringes across the interface behind the loading wave front indicates that no sliding occurs along the interface under symmetric loading.

In both the simulations and the experiments, at the loading wave front there is a cusp in the stress contours at the interface (marked by the arrow A), indicating that the propagation speed is faster along the interface than in the bulk. The cusp in the fringes at the interface in Fig. 7b is also seen when frictional sliding occurs (Figs. 4 and 5). Another characteristic feature is marked by box B in Fig. 7. The curvature of the fringe lines associated with this feature is greater in the computations in Fig. 7a, but this curvature decreases with time. A similar feature, with a curvature closer to what is seen in the computations, is in Fig. 5b. Our simulations indicate that the cusp
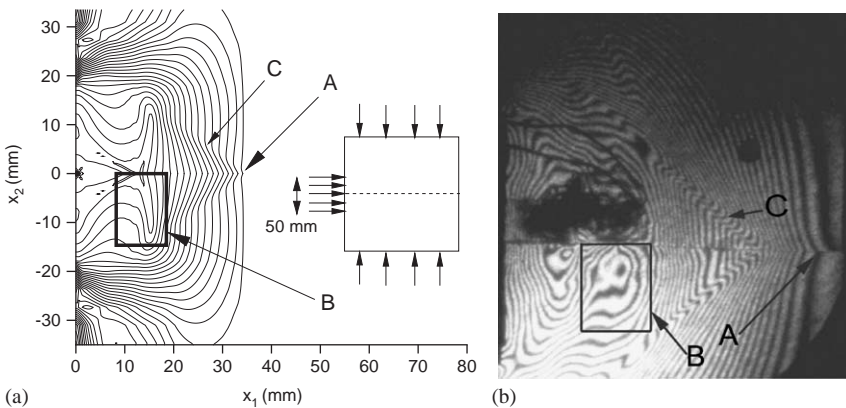

Fig. 7. Isochromatic fringe patterns due to loading symmetric with respect to the interface. (a) Computed isochromatic fringe patterns (contours of $\sigma_1 - \sigma_2$) at $t = 16\,\mu s$ for $\Sigma_0 = 10\,\text{MPa}$, $V_{imp} = 5\,\text{m/s}$, with the configuration analyzed shown in the inset. (b) Experimental isochromatic fringe patterns for $\Sigma_0 = 0\,\text{MPa}$, $V_{imp} = 58\,\text{m/s}$. In (b) the field of view is 130 mm in diameter.

in the fringe line and the feature in box B are a consequence of the impact loading conditions and thus not directly associated with frictional sliding.

A relatively broad head wave that emanates from the interface following the loading wave front is shown by the arrow C. The width of the head wave in the simulations was found to depend on C_n and C_s in Eqs. (7) and (8), and to expand with decreasing applied load. This can be used to set the values of the interface elastic stiffnesses and the values used in most of the calculations here, $C_n = 300\,\text{GPa/m}$ and $C_s = 100\,\text{GPa/m}$, give rather good agreement for symmetrically loaded specimens with Σ_0 in the range 5–40 MPa.

4.2. Case I: crack-like mode

Fig. 8a shows the variation of $\Delta \dot{u}_{\text{slip}}$, and the shear traction, T_s, along the interface at $t = 22\,\mu\text{s}$ (dashed lines) and at $t = 32\,\mu\text{s}$ (solid lines) for Case I ($\Sigma_0 = 6\,\text{MPa}$, $V_{\text{imp}} = 2\,\text{m/s}$). Frictional sliding initiates at the impact edge ($x_1 = 0$) 16 μs after impact. The distributions of $\Delta \dot{u}_{\text{slip}}$ and T_s along the interface are similar at 22 and 32 μs, indicating at least quasi-steady behavior.

Ahead of the frictional sliding tip, $\Delta \dot{u}_{\text{slip}} = 0$. At the tip, $\Delta \dot{u}_{\text{slip}}$ jumps to its peak value of about 7 m/s within two mesh spacings (eight interface integration points) and then gradually reduces to $\approx 5\,\text{m/s}$. As seen in Fig. 8a, the peak value of $\Delta \dot{u}_{\text{slip}}$ gradually increases with time. This behavior is crack-like in that frictional sliding persists at a point on the interface after the sliding front has past that point.

The shear traction steadily increases from the loading wave front, which is at $x_1 = 71\,\text{mm}$ at $t = 32\,\mu\text{s}$, and reaches a maximum value of about 3.9 MPa at the frictional sliding tip after which it decreases to a steady value of 3.6 MPa. The normal traction along the interface gradually increases from its initial value of 6–6.39 MPa at the frictional sliding tip and subsequently decreases to 6.14 MPa along the sliding region. The apparent coefficient of friction, $\mu_{\text{app}} = T_s/T_n$, is
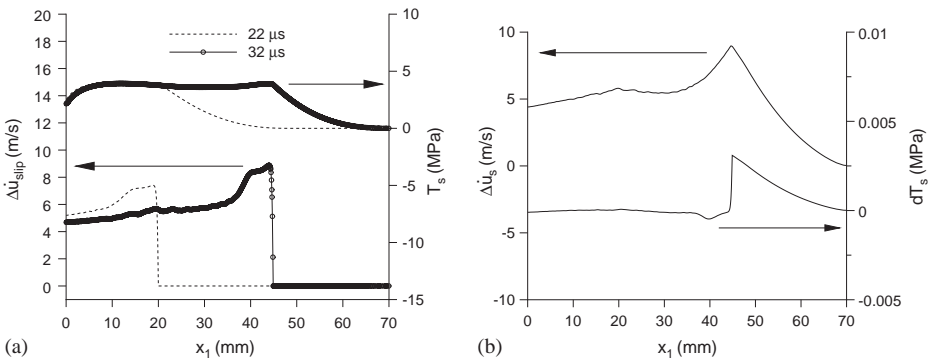

Fig. 8. Distributions along a portion of the interface for Case I—$\Sigma_0 = 6\,\text{MPa}$, $V_{\text{imp}} = 2\,\text{m/s}$. (a) The frictional sliding rate, $\Delta \dot{u}_{\text{slip}}$, and the shear traction, T_s at $t = 22\,\mu\text{s}$ and at $t = 32\,\mu\text{s}$. The symbols mark values at integration points along the interface to illustrate the resolution of the discretization. (b) The shear traction increment, $dT_s = \dot{T}_s\,dt$, and the velocity jump across the interface, $\Delta \dot{u}_s$, at $t = 32\,\mu\text{s}$.

≈ 0.609 at the frictional sliding tip and reduces to 0.585 along the sliding region with small variations. Thus, in this case μ_{app} remains very close to μ_s. The value of T_n itself is nearly constant along the interface, differing by less than 0.6 MPa from $\Sigma_0 = 6$ MPa, except near the impact edge ($0 \leqslant x_1 \leqslant 10$ mm) where the magnitude of T_n decreases.

The actual velocity jump across the interface is $\Delta \dot{u}_s$, which consists of an elastic part in addition to $\Delta \dot{u}_{slip}$. Fig. 8b shows the distribution of $\Delta \dot{u}_s$ as well as the traction increment $dT_s = \dot{T}_s dt$ distribution. Because of the elasticity in the interface constitutive relation, Eq. (8), $\Delta \dot{u}_s$ increases gradually to it peak value, rather than exhibiting a sharp jump. However, behind the frictional sliding tip, $\Delta \dot{u}_s$ and $\Delta \dot{u}_{slip}$ are nearly equal. Consistent with this, since the elastic contribution is $\dot{T}_s/C_s$, $\dot{T}_s \approx 0$ behind the frictional sliding tip.

Isochromatic fringe patterns (contours of $\sigma_1 - \sigma_2$) at $t = 32$ μs are shown in Fig. 9. Behind the loading wave front (which is at 71 mm) a concentration of fringes at 44 mm indicates the location of the frictional sliding tip. A shear Mach cone, formed by a sharp change in fringe density, emanates from the sliding tip at an angle of $34°$. Using $\Delta a/\Delta t = \sin \theta/c_s$, where θ is the Mach angle, gives a tip speed of 2244 m/s which is close to, but less than, the directly calculated tip speed in Fig. 6. Another Mach cone, formed by a more gradual change in fringe density at an angle of $67°$ and, presuming that c_l is the relevant speed of sound for this Mach cone, a propagation speed of 2360 m/s is obtained from $\Delta a/\Delta t = \sin \theta/c_l$. Behind the frictional sliding tip there is no significant stress concentration, indicative of sliding occurring along the interface.

4.3. Case II: pulse-like mode

In Fig. 10a, the variation of the frictional sliding rate, $\Delta \dot{u}_{slip}$, and the shear traction, T_s, along the interface at $t = 32$ μs (dashed lines) and at $t = 34$ μs (solid

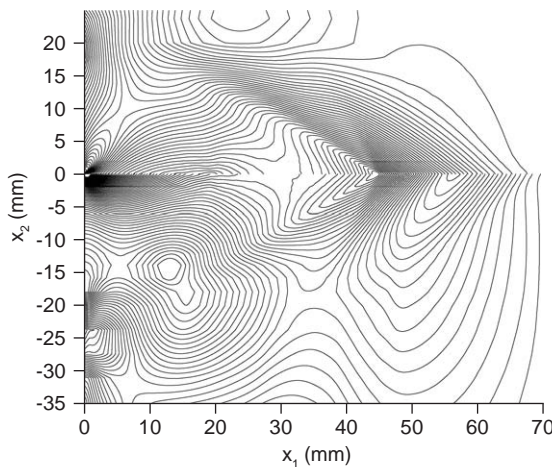Fig. 9. Contours of $\sigma_1 - \sigma_2$ (isochromatic fringe patterns) at $t = 32$ μs for Case I.

lines with circles) are shown for Case II ($\Sigma_0 = 30\,\text{MPa}$, $V_{\text{imp}} = 2\,\text{m/s}$). Frictional sliding initiates at $t = 28\,\mu\text{s}$, which is later than for Case I because the larger compressive stress requires a larger shear stress for initiation. In Case II, frictional sliding occurs in a pulse-like mode which involves a relatively narrow zone (the pulse) where $\Delta\dot{u}_{\text{slip}} > 0$, with $\Delta\dot{u}_{\text{slip}} = 0$ ahead of and behind the pulse. The circles in Fig. 10a show the integration point locations (since $\Delta\dot{u}_{\text{slip}}$ is a constitutive quantity it is stored at interface element integration points) to indicate the extent to which the pulse is resolved; the sharp pulse consists of 9–10 points.

A pulse initiates at the impact edge and as it travels across the interface the peak value of $\Delta\dot{u}_{\text{slip}}$ increases. The pulse profile consists of $\Delta\dot{u}_{\text{slip}}$ gradually increasing from zero to 40 m/s in 4.5 mm after which it sharply rises to 700 m/s over a distance of 0.5 mm and then drops abruptly to zero over a distance of 0.4 mm. Additional pulses initiate and evolve in a similar manner; there are two pulses at $t = 32\,\mu\text{s}$ and three at $t = 34\,\mu\text{s}$.

The shear traction distribution along the interface is also shown in Fig. 10a (note that the range for T_s is larger than in Fig. 8a). At $t = 32\,\mu\text{s}$, the shear traction along the interface gradually increases from zero at the loading wave front (which is at 71 mm) to 18 MPa at the tip of the leading pulse. The value of T_s remains approximately constant over the pulse, abruptly decreases to 14 MPa at the trailing edge of the pulse and then very gradually increases until the second slip-pulse is reached. The variation of the apparent coefficient of friction, $\mu_{\text{app}} = T_s/T_n$, is quite different from that for the crack-like mode. Here, at $t = 32\,\mu\text{s}$, μ_{app} is 0.60 at the front of the frictional sliding tip, very slightly increases to 0.61 over the pulse and then, with the drop in T_s, falls to 0.44. In this case, neither μ_s nor μ_d serve as bounds on the apparent coefficient of friction. Behind the leading pulse the apparent coefficient of friction steadily increases to 0.60 until the trailing pulse is reached. The magnitude of T_n is nearly constant at $\Sigma_0 = 30\,\text{MPa}$ over most of the interface but decreases near the impact edge ($0 \leqslant x_1 \leqslant 10\,\text{mm}$).
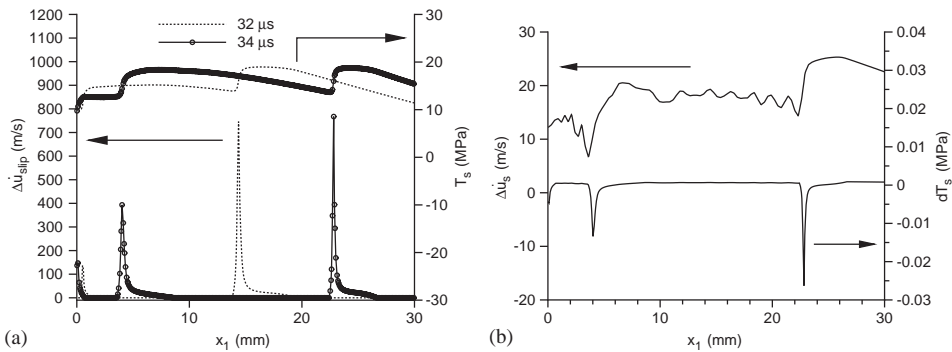

Fig. 10. Distributions along a portion of the interface for Case II—$\Sigma_0 = 30\,\text{MPa}$, $V_{\text{imp}} = 2\,\text{m/s}$. (a) The frictional sliding rate, $\Delta\dot{u}_{\text{slip}}$, and the shear traction, T_s at $t = 32\,\mu\text{s}$ and at $t = 34\,\mu\text{s}$. The symbols mark values at integration points along the interface to illustrate the resolution of the discretization. (b) The shear traction increment, $dT_s = \dot{T}_s\,dt$, and the velocity jump across the interface, $\Delta\dot{u}_s$, at $t = 34\,\mu\text{s}$.

In contrast to the crack-like mode, for the pulse-like mode there is a qualitative difference between the distributions of $\Delta\dot{u}_{\text{slip}}$ and $\Delta\dot{u}_{\text{s}}$ along the interface. As seen in Fig. 10b, which shows distributions of $\Delta\dot{u}_{\text{s}}$ and $dT_{\text{s}} = \dot{T}_{\text{s}}\,dt$ at $t = 34\,\mu\text{s}$, no pulse occurs in the distribution of $\Delta\dot{u}_{\text{s}}$. However, there is an abrupt change in $\Delta\dot{u}_{\text{s}}$ at the location of each pulse. On the other hand, there are pulses in the traction increment dT_{s} and hence in the elastic contribution to $\Delta\dot{u}_{\text{s}} = \dot{T}_{\text{s}}/C_{\text{s}}$. The abrupt change in $\Delta\dot{u}_{\text{s}}$ corresponds to a pulse in $d\Delta\dot{u}_{\text{s}}/dx$, i.e. to a 'weak' pulse as opposed to the 'strong' pulse in $\Delta\dot{u}_{\text{slip}}$.

Isochromatic fringe patterns (contours of $\sigma_1 - \sigma_2$) at $t = 32\,\mu\text{s}$ are shown in Fig. 11 where only the stress contours behind the loading wave front are visible in the region shown. There is a concentration of fringes at approximately $x_1 = 22\,\text{mm}$, which corresponds to the location of the leading slip pulse. The change in the fringe spacing and concentration along a shear Mach line of $26°$ indicates a propagation speed of about $2800\,\text{m/s}$ ($\sin\theta/c_{\text{s}}$). The dense set of fringes near the impact site arises from a slip pulse initiating there.

4.4. Case III: a train of pulses

Fig. 12a shows distributions of frictional sliding rate, $\Delta\dot{u}_{\text{slip}}$, and shear traction T_{s} for a train of pulses ($\Sigma_0 = 10\,\text{MPa}$, $V_{\text{imp}} = 20\,\text{m/s}$). The distributions are shown at two times, at $t = 32\,\mu\text{s}$ and at $t = 33\,\mu\text{s}$. As in Fig. 10a, the circles indicate the positions of the integration points at which $\Delta\dot{u}_{\text{slip}}$ and T_{s} are evaluated. A key difference between the pulses in Case III and those in Case II is that in Case III the peak value of $\Delta\dot{u}_{\text{slip}}$, which is $\approx 120\,\text{m/s}$, does not increase with propagation distance or time. The variations in the peak value of $\Delta\dot{u}_{\text{slip}}$ seen in Fig. 12a is mainly due to some pulses attaining their peak value between the plotted integration points.
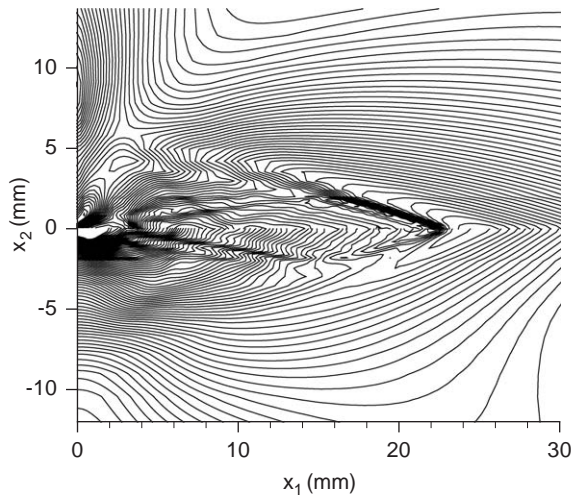

Fig. 11. Contours of $\sigma_1 - \sigma_2$ (isochromatic fringe patterns) at $t = 34\,\mu\text{s}$ for Case II.

Typically, a pulse extends over four elements (16 integration points). The slip pulses at 33 μs (dashed lines) lie on top of the pulses at 32 μs with a one pulse offset, illustrating the self-similar propagation of these pulses.

The shear traction along the interface has a mean value of about 7 MPa with oscillations of 1.5 MPa. The apparent coefficient of friction, $\mu_{app} = T_s/T_n$ oscillates between 0.59 and 0.48 for the slip-pulses behind the leading pulse, but for the leading pulse the maximum is 0.63. The value of T_n is fairly uniform over the interval shown, having a maximum of about 14 MPa at $x_1 \approx 45$ mm and decreasing smoothly to around 11.5 MPa at $x_1 = 30$ mm and $x_1 = 60$ mm, so that the variation in μ_{app} arises principally from the oscillations in T_s. Due to the direct effect in the friction relation, there is a lag between the onset and cessation of frictional sliding and the maximum and minimum values of μ_{app}. The maximum value of 0.59 for μ_{app} is reached 0.43 mm behind the sliding tip for the pulses following the leading pulse and the minimum value of 0.48 occurs 0.25 mm behind the location where $\Delta\dot{u}_{slip}$ peaks (for all pulses, including the leading pulse).

As also seen in Fig. 12a, except for the leading pulse, the shape of the pulses is the same, where the width of the frictional sliding region ($\Delta\dot{u}_{slip} > 0$) is 1.33 mm and the width of the region with $\Delta\dot{u}_{slip} = 0$ is 0.92 mm. The spacing between the pulses is 2.21 mm. The leading pulse has more structure to its front edge, and this structure is preserved as the pulse propagates.

The velocity jump across the interface, $\Delta\dot{u}_s$, and the traction increment $dT_s = \dot{T}_s\,dt$ are shown in Fig. 12b. The traction increment distribution reflects the pulse structure of $\Delta\dot{u}_{slip}$, while the oscillations in $\Delta\dot{u}_s$ are smoother.

Fig. 13 shows the isochromatic fringe patterns (contours of $\sigma_1 - \sigma_2$) at $t = 32$ μs. At the front of the first pulse at 55 mm, a shear Mach wave occurs at 37°, corresponding to a propagation speed of $\approx c_l$. Behind the slip front vortex like stress contours are seen that correspond to the back and front of each pulse together with shear Mach waves at each transition from slip to stick. Behind the propagating front,
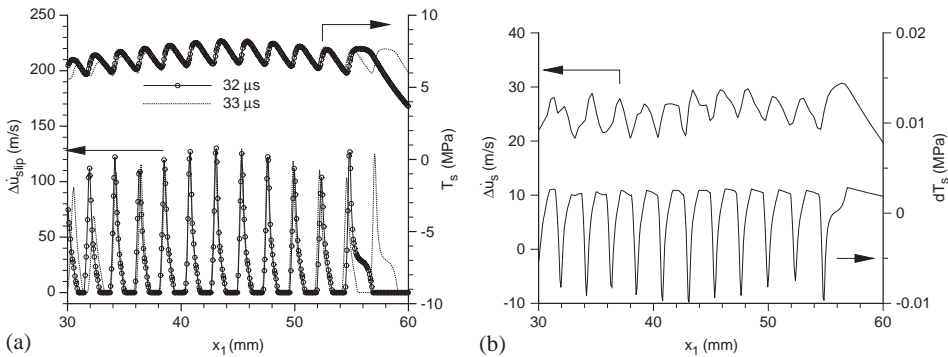

Fig. 12. Distributions along a portion of the interface for Case III—$\Sigma_0 = 10$ MPa, $V_{imp} = 20$ m/s. (a) The frictional sliding rate, $\Delta\dot{u}_{slip}$, and the shear traction, T_s at $t = 32$ μs and at $t = 33$ μs. The symbols mark values at integration points along the interface to illustrate the resolution of the discretization. (b) The shear traction increment, $dT_s = \dot{T}_s\,dt$, and the velocity jump across the interface, $\Delta\dot{u}_s$, at $t = 32$ μs.
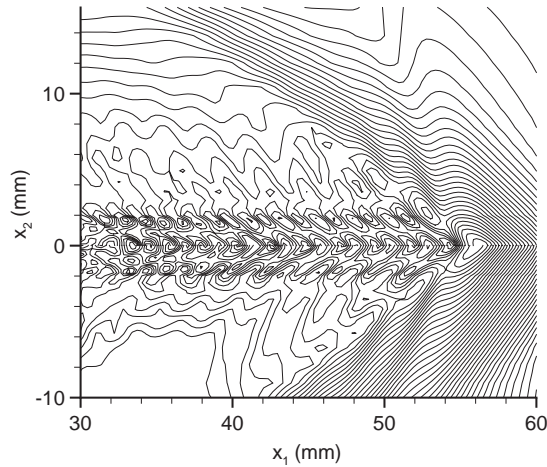
Fig. 13. Contours of $\sigma_1 - \sigma_2$ (isochromatic fringe patterns) at $t = 32\,\mu s$ for Case III.

there is a vortex-like structure. The change in the contours at $x_2 = 2\,mm$ is due to the change in resolution of field quantities associated with the transition from the uniform mesh to the coarser, graduated mesh. This calculation was also carried out for a finer mesh in which the uniform mesh region extends to $x_2 = 4\,mm$, with the element size in the uniform region fixed. The results are essentially unchanged, but the finer mesh results in the details of the stress distribution behind the propagating front being visible over the larger region resolved.

Distributions along the interface of the displacement jump across the interface, Δu_s of the accumulated frictional sliding, $\Delta u_{slip} = \int_0^t \Delta \dot{u}_{slip}\, dt$, and of the apparent coefficient of friction, $\mu_{app} = |T_s/T_n|$, for the crack-like propagation mode (Case I) and for the train of pulses (Case III) are compared in Fig. 14. In both cases, the difference between Δu_s and Δu_{slip} is due to the assumed interface elasticity. In Fig. 14a for Case I, both Δu_s and Δu_{slip} vary smoothly along the slipped surface. For Case III, Fig. 14b, although the displacement jump itself varies smoothly, steps in Δu_{slip} are evident. The elasticity smoothes out the steps in Δu_s along the interface, but these are reflected in the oscillatory distribution of T_s and therefore μ_{app} along the interface.

4.5. Case IV: multiple pulses coalescing to form a crack

In Case IV, the values of the interface elastic constants are $C_n = 30\,GPa/m$ and $C_s = 10\,GPa/m$, one tenth their value in all the other cases. Fig. 15 shows the slip velocity $\Delta \dot{u}_{slip}$ along the interface at 22, 32 and 41 μs. Sliding initiates at 14 μs and at 22 μs (Fig. 15a) three pulses are observed. The tip of the leading pulse is at 18 mm and the distance between the end of the first pulse and the front of the second pulse is 3.4 mm. As in Cases II and III, the leading pulse includes a gradual rising part in the front before there is a steep rise in $\Delta \dot{u}_{slip}$ whereas the
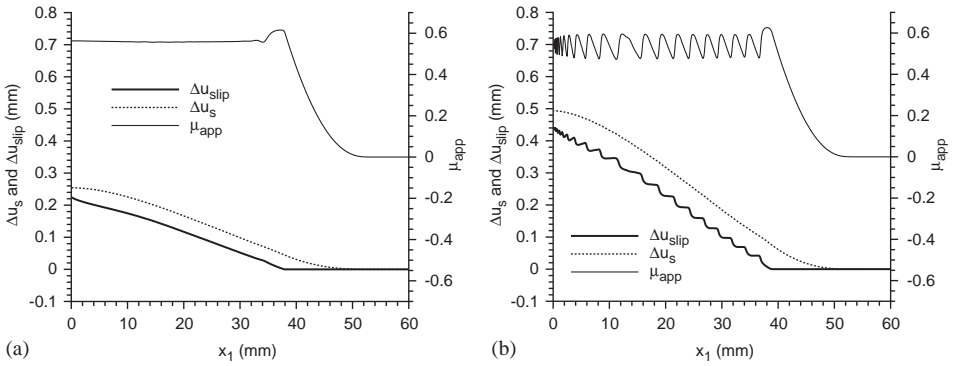
Fig. 14. Distributions of the accumulated frictional sliding, $\Delta u_{\text{slip}} = \int \Delta \dot{u}_{\text{slip}} \, dt$, the displacement jump across the interface, Δu_s and the apparent coefficient of friction, $\mu_{\text{app}} = T_s/T_n$, across the interface at $t = 24\,\mu s$. (a) Case I—$\Sigma_0 = 6\,\text{MPa}$, $V_{\text{imp}} = 2\,\text{m/s}$. (b) Case III—$\Sigma_0 = 10\,\text{MPa}$, $V_{\text{imp}} = 20\,\text{m/s}$.
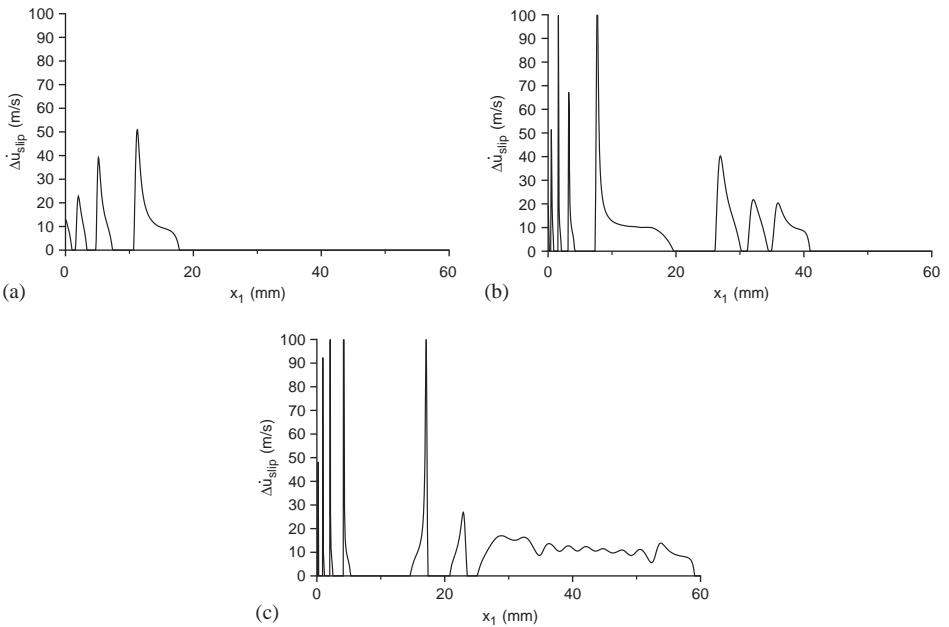

Fig. 15. Distributions of the frictional sliding rate, $\Delta \dot{u}_{\text{slip}}$ for Case IV—$\Sigma_0 = 0.9\,\text{MPa}$, $V_{\text{imp}} = 10\,\text{m/s}$. Also, for Case IV $C_n = 30\,\text{GPa/m}$ and $C_s = 10\,\text{GPa/m}$. (a) $t = 22\,\mu s$. (b) $t = 32\,\mu s$. (c) $t = 48\,\mu s$.

second and third pulses do not exhibit such a gradual rise in $\Delta \dot{u}_{\text{slip}}$. At $32\,\mu s$ in Fig. 15b, the tip of the leading pulse has moved to $41\,\text{mm}$ with the distance between the first and second pulse decreasing to $0.4\,\text{mm}$. During this time the

average speed of the tip of the leading pulse is $\approx c_l$ and the average speed of the second pulse is supersonic, ≈ 2700 m/s. Thus, the second and third sliding pulses which are traveling at supersonic speeds catch up with the lead pulse and coalesce to form a single crack-like sliding region as shown in Fig. 15c (at 41 μs) and then continue to travel at c_l. This crack-like region expands with time as more pulses are generated at the impact edge, travel at supersonic speeds and coalesce with the main sliding region.

Isochromatic fringe patterns (contours of $\sigma_1 - \sigma_2$) are shown in Fig. 16a–c, at 22, 32 and 41 μs, respectively. The contours are shown for $x_2 > 0$ because the Mach line are clearer in this region. At $t = 22$ μs the tip of the leading pulse is at 18 mm as shown by the change in the spacing of the stress contours in Fig. 16a. In Fig. 16b, the tip has moved to 41 mm. There are three regions where an abrupt change in the density of the contours takes place forming three shear Mach lines at three angles to the interface as shown in the inset. The intersections of these lines with the interface are at the locations of the tips of the three sliding pulses shown in Fig. 16b. The shear Mach angles of 34°, 29.3° and 23.4° correspond to propagation speeds of 2190, 2560 and 3160 m/s for the first, second and third pulses, respectively. In Fig. 16c, at 41 μs, the stress contours show a concentration of fringes only at 60 mm corresponding to the sliding tip. At this time the second and third pulses have coalesced with the first pulse to form a crack-like sliding region propagating at the longitudinal wave speed. For $x_1 < 25$ mm there are disturbances that are pulses
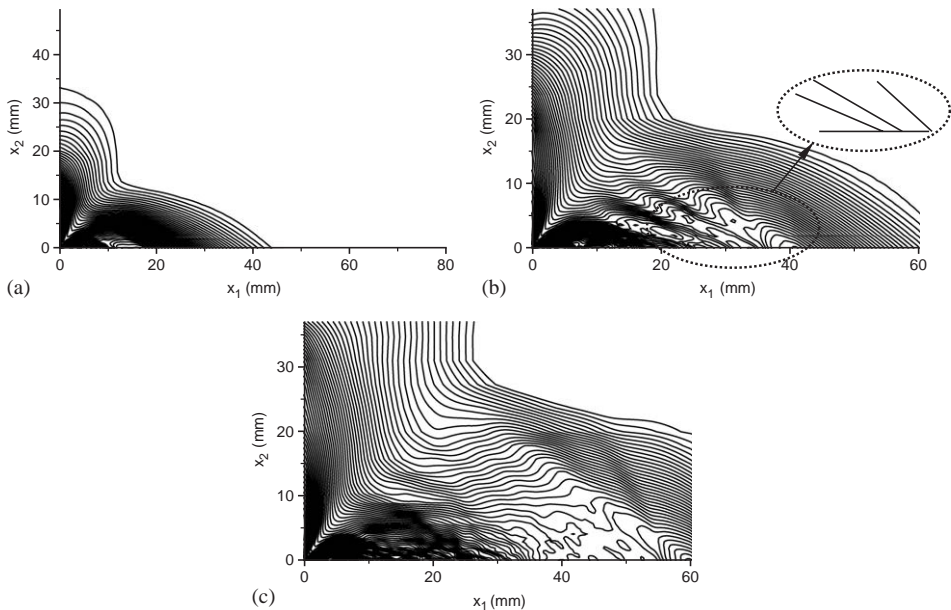

Fig. 16. Contours of $\sigma_1 - \sigma_2$ (isochromatic fringe patterns) for Case IV. The contour lines are drawn to focus on details of the distribution for $x_2 > 0$. (a) $t = 22$ μs. (b) $t = 32$ μs. (c) $t = 48$ μs. The inset in (b) indicates the Mach line orientations.

traveling at supersonic speeds that eventually coalesce with the crack-like sliding region, thereby expanding it.

4.6. Case V: a pulse-like mode followed by a crack-like mode

In Case V, $p = 0.5$ and $V_1 = 1.0$ m/s in Eqs. (15) and (17). Sliding initiates as a slip pulse at 31 μs. Fig. 17 shows the distribution of $\Delta \dot{u}_{slip}$ along the interface at three times; $t = 32$ μs, $t = 38$ μs and $t = 44.6$ μs. Also shown is the distribution of the shear traction, T_s, along the interface at $t = 44$ μs. A growing pulse is obtained with the pulse width decreasing from 8.5 mm at $t = 32$ μs to 2.5 mm at $t = 44$ μs and the peak value of $\Delta \dot{u}_{slip}$ increases from 155 to 392 m/s. The propagation speed of the pulse varies slightly over the range of times in Fig. 17; 2600 m/s at $t = 32$ μs and 2450 m/s at both $t = 38$ μs and $t = 44.6$ μs. After some oscillation behind the growing pulse, $\Delta \dot{u}_{slip}$ is constant at about 21 m/s. The shear traction increases to a maximum value of 23.5 MPa at the tip of the pulse, then drops to 18.5 MPa in the pulse region, after which it remains almost constant at 20 MPa over the rest of the sliding region. The apparent coefficient of friction changes from a maximum value of 0.595 at the sliding tip to a minimum value of 0.47 at the point of maximum frictional sliding rate until it settles at a steady state value of 0.50 along the rest of the sliding surface.

The isochromatic fringe patterns (contours of $\sigma_1 - \sigma_2$) are shown in Fig. 18 at three times of 32, 38 and 44.6 μs. The arrow in each figure points to a line (drawn off the interface) that indicates the width of the pulse and its position along the interface. The pulse width decreases as the crack catches up to the pulse with time and distance. At $t = 38$ μs (Fig. 18b), there are two separate Mach waves corresponding to the slip pulse and the initiation of crack-like slip. As the pulse width diminishes in length the tip of the crack-like region approaches the leading tip of the pulse. From the shear Mach angles, the propagation speed of the back of the pulse in Fig. 18b is approximately 3500 m/s, while the front of the pulse is traveling at about 2600 m/s.
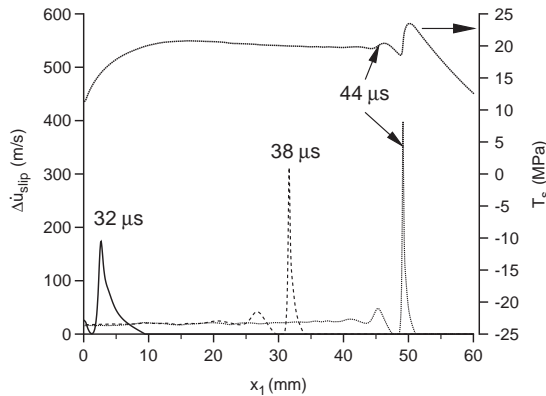

Fig. 17. Distribution of $\Delta \dot{u}_{slip}$ at $t = 32$ μs, $t = 38$ μs and $t = 44$ μs and T_s at $t = 44$ μs along a portion of the interface for Case V—$\Sigma_0 = 40$ MPa, $V_{imp} = 2$ m/s.
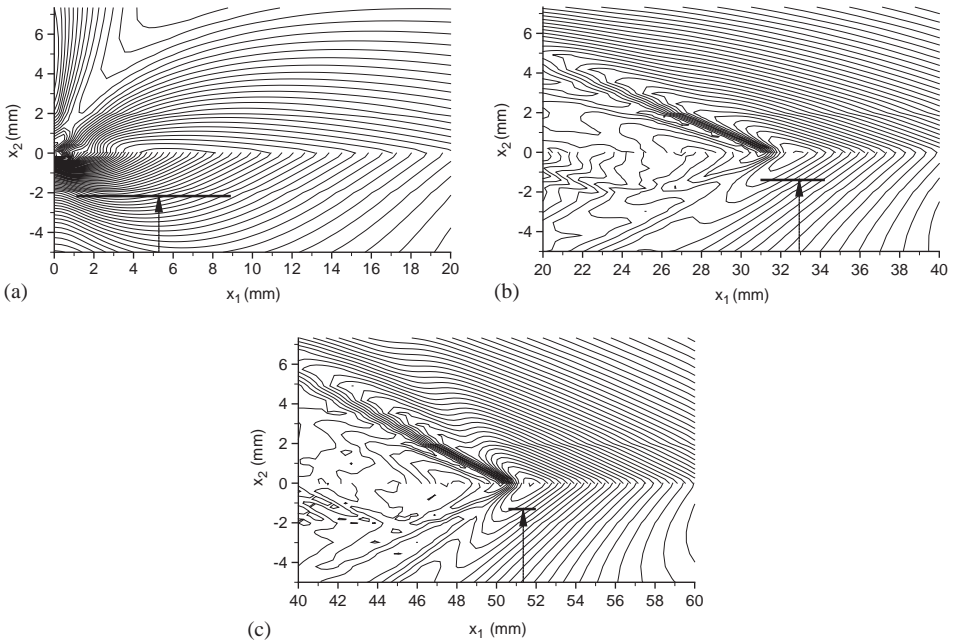
Fig. 18. Contours of $\sigma_1 - \sigma_2$ (isochromatic fringe patterns) for Case V. (a) $t = 32\,\mu s$. (b) $t = 38\,\mu s$. (c) $t = 44.6\,\mu s$. The dark lines indicate the location and width of the pulses in $\Delta\dot{u}_{slip}$ in Fig. 17.

4.7. Dependence of the sliding mode on the initial compressive stress and impact velocity

The dependence of the frictional sliding mode on the initial compressive stress, Σ_0, and the impact velocity, V_{imp}, is shown in Fig. 19. All calculations in Fig. 19 were carried out using the interface friction properties listed in Table 1 and $C_n = 300\,GPa/m$, $C_s = 100\,GPa/m$. The dashed line indicates the boundary between the occurrence of crack-like and pulse-like modes. It is near the dashed line that mixed crack-like and pulse-like modes occur. Quite generally, for low impact velocities and low values of the applied compressive stress, the crack-like mode is obtained. On the other hand, for a high magnitude of the initial compressive stress and a sufficiently low impact velocity, the growing pulse mode occurs.

Fig. 20 illustrates the nature of the transition for a fixed value of Σ_0 and varying V_{imp}, corresponding to the line A in Fig. 19. In Fig. 20, Σ_0 is fixed at 10 MPa and V_{imp} varies between 2 and 40 m/s. Values of $\Delta\dot{u}_s$, $\Delta\dot{u}_{slip}$, T_s and $\mu_{app} = T_s/T_n$ at $x_1 = 16.1$ mm on the interface are plotted as functions of time. With $V_{imp} = 2$ m/s, essentially steady values of the velocity jump across the interface, $\Delta\dot{u}_s$, and the frictional sliding rate, $\Delta\dot{u}_{slip}$, are attained as seen in Fig. 20a and b, respectively. With the impact velocity increased to 10 m/s, the mode has changed to one involving a train of pulses, as seen in Fig. 20b. With a further increase in impact velocity, the pulse amplitude increases as does the pulse frequency. Correspondingly, the
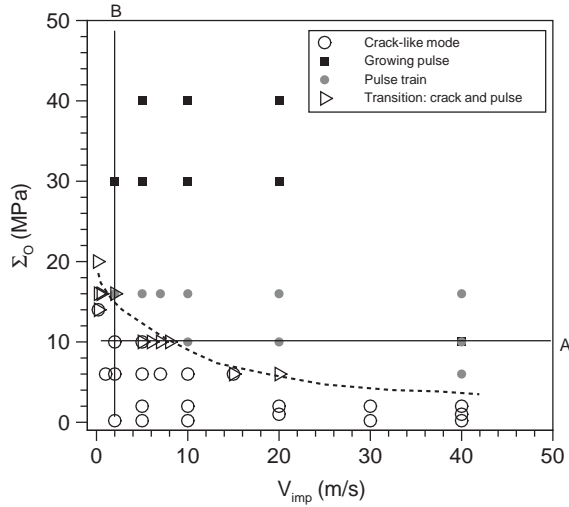
Fig. 19. Dependence of the mode of sliding on the initial compressive stress Σ_0 and the impact velocity V_{imp}. Transition cases where mixed crack-like mode and pulse-like modes occur are shown as triangles.

oscillations in the velocity jump across the interface increase. However, as seen by comparing the response for $V_{imp} = 20\,\text{m/s}$ with $V_{imp} = 40\,\text{m/s}$ in Fig. 20a, the amplitude of the oscillations in $\Delta\dot{u}_s$ do not continue to increase with increasing impact velocity, in contrast to the pulse amplitude in Fig. 20b. Rather, there is an increase in the 'elastic' part of the velocity jump and this is reflected in the increased magnitude of the shear traction T_s in Fig. 20c. The oscillations in the apparent coefficient of friction, $\mu_{app} = T_s/T_n$, increase in magnitude with increasing V_{imp}; μ_{app} changes from an almost steady value of 0.598 at $V_{imp} = 2\,\text{m/s}$ to μ_{app} oscillating between 0.598 and 0.470 at $V_{imp} = 40\,\text{m/s}$. In addition, the frequency of the oscillations in μ_{app} increases with increasing impact velocity.

The nature of the transition for V_{imp} fixed at $2\,\text{m/s}$ and with varying Σ_0, the line B in Fig. 19, is illustrated in Fig. 21. As in Fig. 20, the evolution with time of $\Delta\dot{u}_s$, $\Delta\dot{u}_{slip}$, T_s and μ_{app} at a fixed point along the interface ($x_1 = 16.1\,\text{mm}$) is shown. With increasing initial compressive stress, frictional sliding initiates later (Figs. 21a and b). For both $\Sigma_0 = 6\,\text{MPa}$ and $\Sigma_0 = 10\,\text{MPa}$, crack-like behavior is obtained. The values of $\Delta\dot{u}_s$ and $\Delta\dot{u}_{slip}$ at the beginning of frictional sliding exceed their subsequent steady-state values, which is a consequence of the direct effect in the rate- and state-dependent friction relation. With $\Sigma_0 = 16\,\text{MPa}$, a train of pulses in frictional sliding rate (Fig. 21b) occurs, with oscillations both in $\Delta\dot{u}_s$ (Fig. 21a) and in T_s (Fig. 21c). When the compressive load is increased to $\Sigma_0 = 30\,\text{MPa}$, steeper and narrower pulses are obtained, Fig. 21b, and the peak value of $\Delta\dot{u}_{slip}$ reaches $\approx 820\,\text{m/s}$, much exceeding the scale in Fig. 21b. These slip pulses increase in amplitude as they propagate and the peak $\Delta\dot{u}_{slip}$ can be of the order of c_s. For a sufficiently high value of Σ_0, the closely trailing slip pulses are suppressed. Then, a trailing slip pulse only occurs after some distance and time has passed so that the pulses are well-separated.
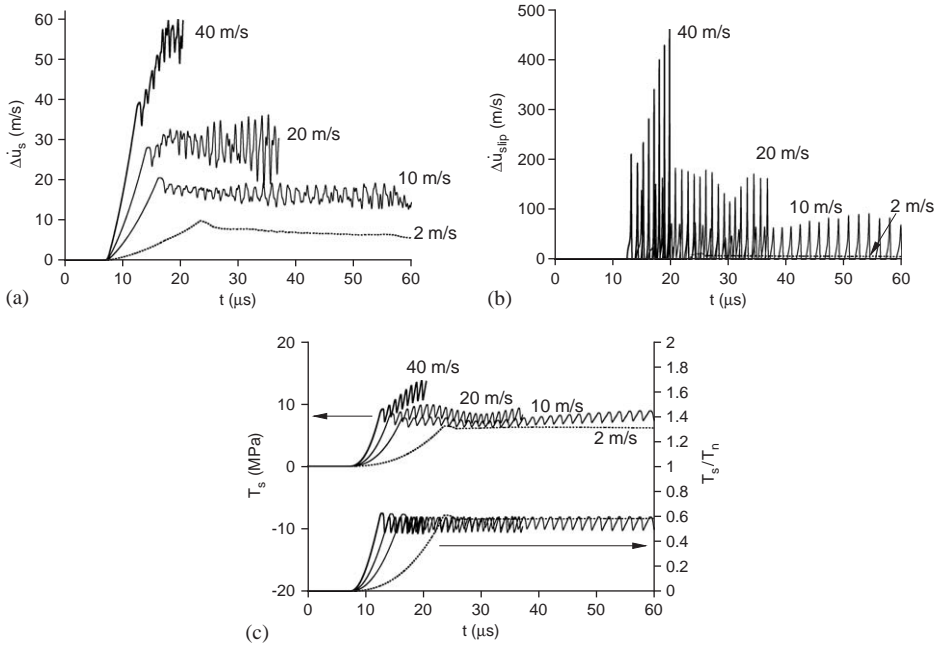
Fig. 20. Effect of varying impact velocity, V_{imp}, on the frictional sliding mode for Σ_0 fixed at 10 MPa. (a) $\Delta\dot{u}_s$, (b) $\Delta\dot{u}_{slip}$, (c) T_s and $\mu_{app} = T_s/T_n$ as functions of time at a fixed point, $x_1 = 16.1$ mm, on the interface.

Such growing pulses have been obtained in studies of sliding between dissimilar elastic solids using rate- and state-dependent friction laws (Ben-Zion and Huang, 2002; Adda-Bedia and Ben Amar, 2003). It is worth noting that if the scale of observation is sufficiently small compared with the pulse spacing, only a single pulse is observed which resembles the slip pulses discussed in relation to earthquakes (Heaton, 1990).

The nature of the slip pulses that occur when Σ_0 is increased (line B in Fig. 19) differ from those obtained when V_{imp} is increased (line A in Fig. 19). With fixed Σ_0, increasing V_{imp} increases the magnitude of the slip pulses while the pulse spacing and the pulse width decrease. For $\Sigma_0 = 16$ MPa, it was found that the pulse width to pulse spacing ratio remained constant with varying V_{imp} and this ratio was equal to one-half. This behavior is analogous to the oscillatory stick–slip behavior observed by Baumberger et al. (1994). The extent to which the pulse width to pulse spacing ratio depends on Σ_0 remains to be determined. In both Figs. 20c and 21c, the peak values of the apparent coefficient of friction do not increase with increasing V_{imp} (Fig. 20c) or Σ_0 (Fig. 21c) even though the magnitude of T_s does, thus implying that there is a corresponding increase in T_n.

To illustrate the evolution of sliding in a transition mode, we describe this evolution for the calculation with $\Sigma_0 = 10$ MPa, $V_{imp} = 7$ m/s (marked by one of the
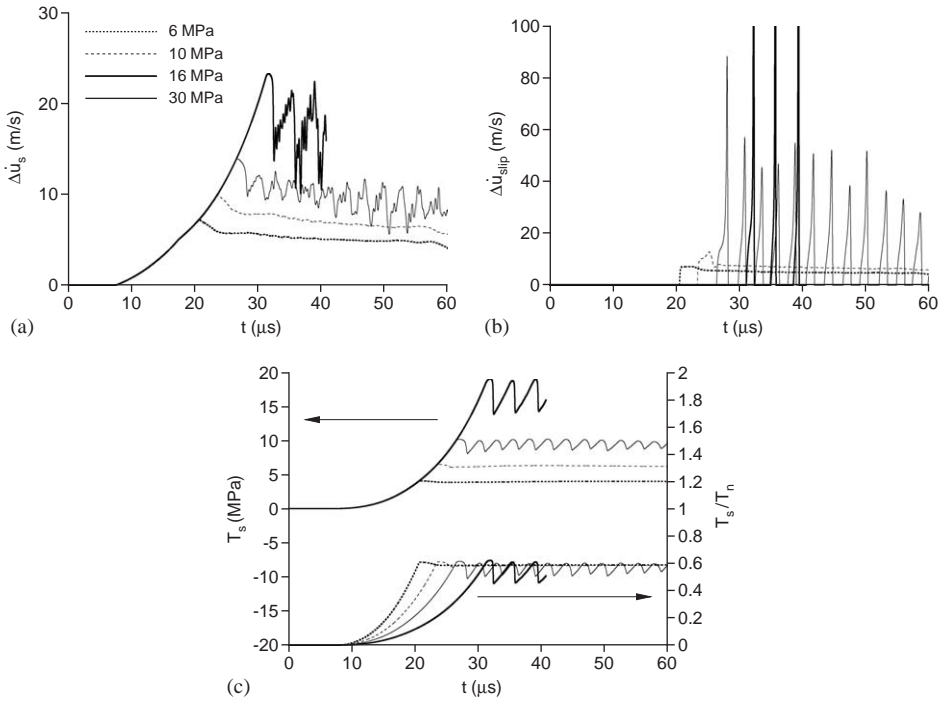
Fig. 21. Effect of varying initial compressive stress, Σ_0, on the frictional sliding mode for V_{imp} fixed at 2 m/s. (a) $\Delta\dot{u}_s$, (b) $\Delta\dot{u}_{slip}$, (c) T_s and $\mu_{app} = T_s/T_n$ as functions of time at a fixed point, $x_1 = 16.1$ mm, on the interface.

triangles in Fig. 19). Oscillations occur in $\Delta\dot{u}_{slip}$ along the interface, with the highest peak near the sliding tip and decreasing in amplitude behind the tip. When sliding has progressed about 50 mm along the interface, the amplitude of the first three oscillations is large enough for $\Delta\dot{u}_{slip}$ to vanish at the crests leading to sticking regions (however the maximum value of $\Delta\dot{u}_{slip}$ generally remains a small fraction of an elastic wave speed). The amplitude of the following oscillations is much smaller and sticking does not occur. Thus, we obtain a crack-like sliding region following three slip-pulses of decreasing magnitude.

Other loading combinations of Σ_0 and V_{imp} on the transition line in Fig. 19, lead to similar oscillations in the slip rate or to unsteady behaviors, such as mixed crack-like and pulse-like sliding modes that evolve with both time and distance. This behavior is reminiscent of that found in the analysis of spring-slider system obeying a rate- and state-dependent friction law (Ruina, 1983; Gu et al., 1984) where it was shown that the transition from steady sliding to stick–slip goes through several oscillations, period doubling and self-sustained periodic oscillations. Gu and Wong (1991, 1994) also found this transition to be dependent on the load point driving velocity in addition to the stiffness and constitutive parameters.

5. Discussion

The experiments and calculations for symmetric loading with no sliding, permit the features of the response associated with sliding to be identified. Also, the good agreement between the experiments and the calculations for symmetric loading provides confidence that the wave propagation aspects of the experiments are well-represented in the calculations. Features that are common between the symmetric loading experiments and the corresponding calculations include the cusp in the photoelastic fringes at the interface, the formation of a head wave emanating from the loading wave front and the distortions in the photoelastic stress field behind the loading wave due to the trapezoidal nature of the imposed loading.

A guideline for assessing mesh resolution (Zheng and Rice, 1998) is that the mesh spacing (0.3 mm along the interface in the uniform mesh region) should be significantly less than a characteristic length, h^*, associated with the friction law,

$$h^* = |2GL_0/[\pi \Delta \dot{u}_{\text{slip}} (\mathrm{d}\tau_{\text{ss}}/\mathrm{d}\Delta \dot{u}_{\text{slip}})]|$$

where G is the shear modulus and τ_{ss} is the shear stress under steady-state sliding. For a normal stress of 10 MPa, h^* attains its minimum of 0.81 mm for $\Delta \dot{u}_{\text{slip}} = V_1 = 26$ m/s. Using $\Delta \dot{u}_{\text{slip}} = V_1 = 7$ m/s as a representative value for Case I, $h^* = 1.8$ mm. For Case IV, where the normal stress is ≈ 1 MPa and $\Delta \dot{u}_{\text{slip}}$ ranges from about 10–100 m/s, the minimum value of h^* is 8.1 mm and for much of the velocity range is significantly greater than that. It is worth noting that it is for Case IV that a supersonic pulse is obtained. For the other cases, h^* typically has values between those for Cases I and IV.

Several calculations were carried out to assess the mesh dependence of the results. For Case I (crack-like mode) and for Case II (pulse-like mode), calculations were carried out with the mesh spacing halved along the interface (0.15 mm in the uniform region) so that the number of elements was doubled. For Case I, with the finer mesh the transition region at the sliding tip consisted of four elements (16 integration points) as opposed to two elements (8 integration points) with the coarser mesh. The values of $\Delta \dot{u}_{\text{slip}}$ obtained from the two calculations nearly coincide. The mean values of the curves of V_{tip} versus time computed using the finer mesh also essentially coincide with the curves in Fig. 6 but the oscillations about the mean differ somewhat. In addition, the effect of mesh size was further explored for a crack-like mode and a pulse like mode using frictional parameters that differ from those used in Cases I and II. The reference mesh shown in Fig. 1b and two other meshes were used for this. All the meshes have the smallest elements near the interface and the impact edge as for the reference mesh in Fig. 1b. The coarse mesh consisted of 1152 elements and 4812 degrees of freedom, with the smallest element size 2.1 mm × 1.0 mm. The fine mesh consisted of 56,832 elements and 229,364 degrees of freedom, with the smallest element size 0.075 mm × 0.1 mm. The slip rate at a point along the interface was plotted as a function of time for both meshes. In the calculation with the crack-like sliding mode, the results from all three calculations are in very good agreement for the propagation speed except that increased fluctuations around a steady slip rate occur with the coarse mesh. For the pulse-like mode calculation, there is only a small

difference between the calculations using the three meshes for the predicted magnitude and timing of the pulses. For the train of pulses sliding mode, calculations were carried out for finite element meshes with interface mesh spacings of 0.15 mm, 0.30 mm and 0.40 mm. The pulse shape, width and spacing were virtually identical in the three calculations, with a typical slip pulse in these meshes spanning 37, 19 and 14 integration points, respectively.

The calculations are carried out neglecting geometry changes so that the displacement jumps Δu_n and Δu_s pertain to differences between points that are on opposite sides of the interface in the initial configuration. Possible effects of accounting for geometry changes, with the jumps then pertaining to points on opposite sides of the interface in the current configuration, remain to be determined. It is however worth noting that at least in Fig. 14 when Δu_s is relatively large, the shear traction is relatively uniform.

The values used for the interface stiffnesses C_n and C_s in Eqs. (7) and (8) play a significant role both for symmetric loading (with no sliding) and for asymmetric loading (with frictional sliding). The values used in most of the calculations, $C_n = 300\,\mathrm{GPa/m}$ and $C_s = 100\,\mathrm{GPa/m}$, give rather good agreement with the experiments for symmetrically loaded specimens where sliding does not occur. In order to assess the dependence of the sliding mode on the interface stiffness values employed, asymmetric loading calculations were carried out using various values of C_n and C_s. For given values of Σ_0 and V_{imp}, the frictional sliding mode that occurs depends on C_n and C_s. With $C_n = 3000\,\mathrm{GPa/m}$ and $C_s = 1000\,\mathrm{GPa/m}$, only crack-like behavior was obtained for the range of values of Σ_0 and V_{imp} used in Fig. 19. On the other hand, various calculations were carried out with $C_n = 30\,\mathrm{GPa/m}$ and $C_s = 10\,\mathrm{GPa/m}$ and a train of pulses was not obtained, although as shown for Case IV pulses coalescing to form a crack-like sliding mode did occur. Also, pulse steepening became more pronounced when C_n and C_s were decreased.

The elasticity of the interface plays a fundamental role because the frictional slip $\Delta \dot{u}_{slip}$ is an internal variable determined by the frictional law (analogous to the plastic strain rate in plasticity theory). The observable quantity is the jump in displacement rate across the interface, $\Delta \dot{u}_s$. The pulses occur in $\Delta \dot{u}_{slip}$ not in $\Delta \dot{u}_s$ and, hence, according to our numerical results, are not directly observable in terms of a velocity jump distribution along an interface. What is observable is a pulse-type traction rate distribution (Figs. 10b and 12b). At a given spatial location, the oscillatory nature of the pulse-like modes is seen in the time evolution of $\Delta \dot{u}_s$ (Fig. 20a).

Calculations modeling dynamic slip in earthquakes, e.g. Cochard and Madariaga (1994, 1996), Perrin et al. (1995), Beeler and Tullis (1996) (see also Ben-Zion, 2001; Rice, 2001; Nielsen and Madariaga, 2003), exhibit both crack-like and pulse-like sliding modes. In analyzing conditions that set the mode of sliding, Zheng and Rice (1998) considered the special case of identical material properties on both sides of the slip surface. Specifically, Zheng and Rice (1998) considered elastic half-spaces that are subject to a uniform shear stress τ_0^b outside a perturbed region where slip nucleates. The criterion delineating between crack-like and pulse-like sliding involves the magnitude of τ_0^b, the elastic moduli and shear wave speed of the half-spaces, the sliding speed and the sliding speed dependence of the interface friction law. The

criterion of Zheng and Rice (1998) predicts that low values of τ_0^b favor pulse-like sliding and higher values crack-like sliding.

The circumstances considered here are quite different from those in Zheng and Rice (1998). In particular, it is important to note that the parameters in Fig. 19 are the initial *compressive* stress and the *impact* velocity. In this parameter space, a clear demarcation is found between the regime where the crack-like and pulse-like modes occur; a low initial compressive stress and/or a low impact velocity favor the crack-like mode.

The experiments and calculations exhibit a variety of common features including:

(i) Direct calculation from the time history of the position of the sliding tip and Mach lines in the contours of $\sigma_1 - \sigma_2$ indicate that the sliding tip travels at a speed greater than $\sqrt{2}c_s$ and that a trailing pulse travels faster than c_l.
(ii) The fringe patterns in front of the sliding region have similar characteristic shapes.
(iii) Crack-like sliding occurs at low impact velocities and a sliding mode with a pulse is obtained at higher impact velocities.
(iv) Two shock waves eventually merge into a single shock wave as the trailing shock catches up to the leading one. The tip of the trailing pulse travels at a speed exceeding c_l.

The calculations exhibit two sliding modes with two approaching shock waves. One involves trailing pulses traveling faster than the leading pulse that eventually coalesce to form one sliding region (Figs. 15 and 16). The other involves a steepening and narrowing pulse followed by a crack-like sliding region (Figs. 17 and 18).

There is some evidence in other contexts regarding the range of sliding modes that emerge from our calculations, more specifically regarding the pulse and pulse train modes of frictional sliding. Rubio and Galeano (1994) carried out experiments on sheared gels sliding along smooth glass surfaces and observed sliding via propagation of a quasi-periodic pattern of sliding zones of finite width separated by non-moving regions, having a propagation speed of the order of c_l of the gel. This is consistent with our observations of relative speeds of pulse propagation that are three order of magnitude higher than the imposed impact velocities. The experiments of Rubio and Galeano (1994) motivated an analysis by Caroli (2000) of sliding of a viscoelastic solid on a rigid substrate with a rate and state friction law that showed a pulse train. Sliding between a rectangular polyurethane slab and a compressed araldite plate was studied experimentally by Mouwakeh et al. (1991). The velocity measured at a fixed spatial point was strongly oscillatory. Also, the measured traction exhibited oscillations. The traction versus time curve in Mouwakeh et al. (1991) resembles one of the oscillatory curve in Fig. 21c. The velocity versus time curve is qualitatively similar to the intermediate curves in Fig. 21b. However it is unclear whether $\Delta\dot{u}_{slip}$ or $\Delta\dot{u}_s$ is plotted in Mouwakeh et al. (1991, Fig. 5a).

Fiber pull-out experiments exhibit a variety of complex frictional phenomena, e.g. Tsai and Kim (1996) and Li et al. (2002). In particular, Tsai and Kim (1996) observed three frictional sliding modes: steady sliding of the entire contact surface, stick–slip sliding of the entire contact surface, and sliding through the generation of concentrated

sliding pulses. In one set of experiments, with sliding along the entire contact surface, the pull-out force was steady for a low interface pressure and was oscillatory for a high interface pressure, analogous to the behavior in our calculations where a crack-like sliding mode occurs for low values of Σ_0 and a pulse-like mode for high values of Σ_0. However, Tsai and Kim (1996) found that the oscillation amplitude decreased with increasing pull-out speed. This trend, also found in Baumberger et al. (1994) and Povirk and Needleman (1993), under quasi-static loading conditions, is opposite to what occurs in our analyses under dynamic loading conditions.

Brune et al. (1993) and Anooshehpoor and Brune (1994) observed two modes of sliding along the interface between identical foam rubber blocks; one involving wrinkle-like waves and the other a crack-like sliding mode. Characteristics of the wrinkle-like wave mode in these experiments are similar to those obtained for slip-pulses in our calculations; for example, an increasing normal component of particle motion with increasing normal stress which is analogous to the slip-pulse amplitude increasing with Σ_0 in our calculations. Interestingly, it was found that the frictional heating did not change with shear stress in the wrinkle-like wave mode whereas it increased linearly with shear stress in the crack-like mode (see also Andrews and Ben-Zion, 1997, Fig. 12). In experiments on sliding of two dissimilar blocks of foam rubber, Anooshehpoor and Brune (1999) observed that sliding occurred through a series of multiple opening pulses. They also found that the sharpness and the amplitude of the pulses either increased or decreased with time and was not steady. Such opening pulses, often referred to as Schallamach (1971) waves, have been observed experimentally in various bimaterial systems (e.g. Schallamach, 1971; Anooshehpoor and Brune, 1999) and in simulations (Coker et al., 2003). There is evidence for slip pulses, on which attention is focused here, in the experiments of Mouwakeh et al. (1991) and Tsai and Kim (1996).

Fig. 14 shows that the displacement distribution from a pulse train slip mode and from a crack-like slip mode are quite similar. This might be the reason that there is ample experimental evidence of slip pulses in soft materials such as gels, whereas there is no conclusive experimental evidence for slip pulses in engineering materials where the displacement magnitudes are very small compared to those in soft materials. However, the shear traction distribution along the interface in Fig. 14 does provide an indicator of the slip-mode. The variation of the shear resistance and the step increase in displacement in Fig. 14 is similar to the response seen in rock friction experiments (Tullis, 1996) and in fiber pull-out experiments (Tsai and Kim, 1996). Since the resulting slip from a train of pulses is hard to distinguish from that occurring with the crack-like slip mode, our results suggest the possibility that slip pulses may be more common than previously appreciated. It remains to be determined whether there is a significant difference between the heat generation associated with the pulse-train mode and that associated with the crack-like mode.

6. Conclusions

Frictional sliding between two Homalite plates subject to a compressive stress was investigated both experimentally and computationally. Sliding under shear loading

was induced by impacting one plate parallel to the interface. The experiments yield information on the sliding speed and the stress state in the material using dynamic photoelasticity. A plane stress initial/boundary value problem simulating the experiments is analyzed using a framework where sliding is modeled by a rate- and state-dependent frictional interface constitutive relation.

- The experiments exhibit both pulse-like and crack-like modes of sliding.
- In the experiments, the speed of the leading pulse or the leading edge of the crack-like sliding region ranges from somewhat above $\sqrt{2}c_s$ to c_l. This propagation speed increases with increasing impact velocity and decreasing compressive stress. A speed exceeding c_l was seen for a trailing pulse.
- A variety of frictional sliding modes were obtained in the calculations, depending on the initial compressive stress, the impact velocity and the interface characterization: a crack-like mode; a pulse-like mode with well-separated pulses that increase in amplitude; and a train of pulses that propagate with an essentially constant amplitude. In addition, combinations of these modes occurred as well as transitions between modes. This variety of sliding modes emerges even though there is no elastic mismatch across the interface.
- The slip resulting from the pulse-train mode and that resulting from the crack-like mode are hard to distinguish.
- In all calculations the speed of the leading pulse or the leading edge of the crack-like sliding region exceeds $\sqrt{2}c_s$ and is close to (or slightly exceeds) c_l. As in the experiments, trailing pulses with a speed exceeding c_l are found.
- The elasticity of the interface plays a significant role in setting the mode of sliding.
- The range of sliding modes obtained appear to be generic, arising in a wide variety of configurations and applications, and at a wide variety of size scales.

Acknowledgements

Appendix. Time integration of the friction law

The equations are integrated in time using of a rate tangent method (Peirce et al., 1984) and automatic time step control. The sliding velocity, $\Delta\dot{u}_{slip}$, in the interval

$[t, t + dt]$, is expressed as a linear combination of its values at t and $t + dt$ via

$$\Delta \dot{u}_{\text{slip}} = (1 - \gamma)\Delta \dot{u}_{\text{slip}}(t) + \gamma \Delta \dot{u}_{\text{slip}}(t + dt), \tag{22}$$

where γ is a chosen integration parameter that can range in value from 0 to 1.

A first order expansion of $\Delta \dot{u}_{\text{slip}}$ in terms of T_s, θ_1, θ_2, and θ_0 gives

$$\Delta \dot{u}_{\text{slip}}(t + dt)$$
$$= \Delta \dot{u}_{\text{slip}}(t) + dt\left(\frac{\partial \Delta \dot{u}_{\text{slip}}}{\partial |T_s|}\text{sgn}(T_s)\dot{T}_s + \frac{\partial \Delta \dot{u}_{\text{slip}}}{\partial \theta_0}\dot{\theta}_0 + \frac{\partial \Delta \dot{u}_{\text{slip}}}{\partial \theta_1}\dot{\theta}_1 + \frac{\partial \Delta \dot{u}_{\text{slip}}}{\partial \theta_2}\dot{\theta}_2\right), \tag{23}$$

where all derivatives are evaluated at t.

Combining (23) with (8) gives

$$\dot{T}_s = C_s^{\text{tan}}\Delta \dot{u}_s - \dot{R}_p, \tag{24}$$

with

$$C_s^{\text{tan}} = \frac{C_s}{1 + \gamma \, dt \dfrac{\partial \Delta \dot{u}_{\text{slip}}}{\partial |T_s|} C_s} \tag{25}$$

and

$$\dot{R}_p = C_s^{\text{tan}}\text{sgn}(T_s)\left(\Delta \dot{u}_{\text{slip}}(t) + \gamma \, dt \frac{\partial \Delta \dot{u}_{\text{slip}}}{\partial \theta_0}\dot{\theta}_0 + \frac{\partial \Delta \dot{u}_{\text{slip}}}{\partial \theta_1}\dot{\theta}_1 + \frac{\partial \Delta \dot{u}_{\text{slip}}}{\partial \theta_2}\dot{\theta}_2\right). \tag{26}$$

The partial derivatives in Eq. (26) are

$$\frac{\partial \Delta \dot{u}_{\text{slip}}}{\partial |T_s|} = \frac{mV_0\beta^{m-1}}{-T_n g(\theta_0)}, \tag{27}$$

$$\frac{\partial \Delta \dot{u}_{\text{slip}}}{\partial \theta_0} = \frac{-mV_0\beta^m}{g(\theta_0)}\frac{\partial g}{\partial \theta_0}, \tag{28}$$

$$\frac{\partial \Delta \dot{u}_{\text{slip}}}{\partial \theta_1} = \frac{\partial \Delta \dot{u}_{\text{slip}}}{\partial \theta_2} = -\frac{mV_0\beta^m}{(\theta_1 + \theta_2)}, \tag{29}$$

where $g(\theta_0)$ and β are given by Eqs. (15) and (18) and

$$\frac{\partial g}{\partial \theta_0} = \frac{(\mu_s - \mu_d)\dfrac{p}{\theta_0}\left(\dfrac{L_0}{V_1\theta_0}\right)^p \exp\left[-\left(\dfrac{L_0}{V_1\theta_0}\right)^p\right]}{Q^{1/m}} + \mu^*\frac{L_0}{mV_0\theta_0^2}\frac{1}{Q^{1/m+1}}. \tag{30}$$

Here,

$$Q = \frac{L_0}{V_0\theta_0} + 1, \tag{31}$$

$$\mu^* = \mu_d + (\mu_s - \mu_d)\exp\left[-\left(\frac{L_0}{V_1\theta_0}\right)^p\right]. \tag{32}$$

The integral along the interface in Eq. (1) is written as the sum over linear displacement interface elements. All field quantities and constitutive state variables are known at time t. Also, the values of $\Delta\dot{u}_n$ and $\Delta\dot{u}_s$ have been determined from solving Eq. (9). Thus, Δu_n and Δu_s are know at time $t + dt$. Then, at a given integration point along the interface:

1. Calculate $\Delta\dot{u}_s = [\Delta u_s(t + dt) - \Delta u_s(t)]/dt$ and $\Delta\dot{u}_n = [\Delta u_n(t + dt) - \Delta u_n(t)]/dt$.
2. If $\Delta u_n(t + dt) > \Sigma_0/C_n$ then set $T_n = T_s = 0$ and go to the next integration point.
3. Using the values for the state variables at time t, calculate $g(\theta_0)$.
4. Compute

$$\beta = \frac{|T_s|}{g(\theta_0)(\theta_1 + \theta_2)}. \tag{33}$$

5. If $\beta < 1$ then $\Delta\dot{u}_{slip} = 0$. Go to 7.
6. If $\beta > 1$ calculate C_s^{tan} and $\dot{R}_p$ in Eq. (24).
7. Update the tractions and state variables via

$$T_n^{k+1} = T_n^k + \dot{T}_n\, dt, \tag{34}$$
$$T_s^{k+1} = T_s^k + \dot{T}_s\, dt, \tag{35}$$
$$\theta_i^{k+1} = \theta_i^k + \dot{\theta}_i\, dt, \quad i = 0, 1, 2. \tag{36}$$

References

Abraham, F.F., 2001. The atomic dynamics of fracture. J. Mech. Phys. Solids 49, 2095–2111.

Abraham, F.F., Gao, H.J., 2000. How fast can cracks propagate? Phys. Rev. Lett. 84, 3113–3116.

Adams, G.G., 1995. Self-excited oscillations of two elastic half-spaces sliding with a constant coefficient of friction. J. Appl. Mech. 62, 867–872.

Adda-Bedia, M., Ben Amar, M., 2003. Self- sustained slip pulses of finite size between dissimilar materials. J. Mech. Phys. Solids 51, 1849–1861.

Andrews, D.J., 1976. Rupture velocity of plain strain shear cracks. J. Geophys. Res. 81, 5679–5687.

Andrews, D.J., Ben-Zion, Y., 1997. Wrinkle-like slip pulse on a fault between different materials. J. Geophys. Res. 102, 553–571.

Anooshehpoor, A., Brune, J.N., 1994. Frictional heat-generation and seismic radiation in a foam rubber model of earthquakes. Pure Appl. Geophys. 142, 735–747.

Anooshehpoor, A., Brune, J.N., 1999. Wrinkle-like Weertman pulse at the interface between two blocks of foam rubber with different velocities. Geophys. Res. Lett. 26, 2025–2028.

Archuleta, R.J., 1984. A faulting model for the 1979 imperial valley earthquake. J. Geophys. Res. 89, 4559–4585.

Baumberger, T., Heslot, F., Perrin, B., 1994. Crossover from creep to inertial motion in friction dynamics. Nature 367, 544–547.

Beeler, N.M., Tullis, T.E., 1996. Self-healing slip pulses in dynamic rupture models due to velocity-dependent strength. Bull. Seismol. Soc. Am. 86, 1130–1148.

Belytschko, T., Chiapetta, R.L., Bartel, H.D., 1976. Efficient large scale nonlinear transient analysis by finite elements. Int. J. Numer. Methods Eng. 10, 579–596.

Ben-Zion, Y., 2001. Dynamic ruptures in recent models of earthquake faults. J. Mech. Phys. Solids 49, 2209–2244.

Ben-Zion, Y., Andrews, D.J., 1998. Properties and implications of dynamic rupture along a material interface. Bull. Seismol. Soc. Am. 88, 1085–1094.

Ben-Zion, Y., Huang, Y., 2002. Dynamic rupture on an interface between a compliant fault zone layer and a stiffer surrounding solid. J. Geophys. Res. 107, B2 article no 2042.

Ben-Zion, Y., Rice, J.R., 1997. Dynamics simulations of slip on a smooth fault in an elastic solid. J. Geophys. Res. 102, 17,771–17,1784.

Bizzarri, A., Cocco, M., Andrews, D.J., Boschi, E., 2001. Solving the dynamic rupture problem with different numerical approaches and constitutive laws. Geophys. J. Int. 144, 656–678.

Bouchon, M., Bouin, M.P., Karabulut, H., Toksöz, M.N., Dietrich, M., Rosakis, A.J., 2001. How fast is rupture during an earthquake? New sights from the 1999 Turkey earthquakes. Geophys. Res. Lett. 28, 2723–2726.

Bouchon, M., Vallee, M., 2003. Observation of long supershear rupture during the magnitude 8.1 Kunlunshan earthquake. Science 301, 824–826.

Broberg, K.B., 1995. Intersonic mode II crack expansion. Arch. Mech. 47, 859–871.

Broberg, K.B., 1996. How fast can a crack go? Mater. Sci. 32, 80–86.

Broberg, K.B., 1999. Cracks and Fracture. Academic Press, London.

Brune, J.N., Brown, S., Johnson, P.A., 1993. Rupture mechanism and interface separation in foam rubber models of earthquakes—a possible solution to the heat-flow paradox and the paradox of large overthrusts. Tectonophys. 218, 59–67.

Burridge, R., 1973. Admissible speeds for plane strain self-similar shear cracks with friction but lacking cohesion. Geophys. J. Roy. Astron. Soc. 35, 439–455.

Caroli, C., 2000. Slip pulses at a sheared frictional viscoelastic/nondeformable interface. Phys. Rev. E 62, 1729–1737.

Cochard, A., Madariaga, R., 1994. Dynamic faulting under rate-dependent friction. Pure Appl. Geophys. 142, 419–445.

Cochard, A., Madariaga, R., 1996. Complexity of seismicity due to highly rate-dependent friction. J. Geophys. Res. Solid Earth 101, 25,321–25,336.

Cochard, A., Rice, J.R., 2000. Fault rupture between dissimilar materials: Ill-posedness, regularization, and slip-pulse response. J. Geophys. Res. 105, 25,891–25,907.

Coker, D., Rosakis, A.J., 2001. Experimental observations of intersonic crack growth in asymmetrically loaded unidirectional composite plates. Philos. Mag. A 81, 571–595.

Coker, D., Rosakis, A.J., Needleman, A., 2003. Dynamic crack growth along a polymer composite-homalite interface. J. Mech. Phys. Solids 51, 425–460.

Dieterich, J.H., 1979. Modeling of rock friction 1. Experimental results and constitutive equations. J. Geophys. Res. 84, 2161–2168.

Dunham, E.M., Favreau, P., Carlson, J.M., 2003. A supershear transition mechanism for cracks. Science 299, 1557–1559.

Freund, L.B., 1998. Dynamic Fracture Mechanics. Cambridge University Press, Cambridge, UK.

Gao, H.J., Huang, Y., Abraham, F.F., 2001. Continuum and atomistic studies of intersonic crack propagation. J. Mech. Phys. Solids 49, 2113–2132.

Gu, Y.J., Wong, T.F., 1991. Effects of loading velocity, stiffness, and inertia on the dynamics of a single degree of freedom spring-slider system. J. Geophys. Res. 96, 21,677–21,691.

Gu, Y.J., Wong, T.F., 1994. Development of shear localization in simulated quartz gouge—effect of cumulative slip and gouge particle-size. Pure Appl. Geophys. 143, 387–423.

Gu, J.-C., Rice, J.R., Ruina, A.L., Tse, S.T., 1984. Slip motion and stability of a single degree of freedom elastic system with rate and state dependent friction. J. Mech. Phys. Solids 32, 167–196.

Hao, S., Wing, K.L., Klein, P.A., Rosakis, A.J., 2004. Modeling and simulation of intersonic crack growth. Int. J. Solids Struct. 41, 1773–1799.

Heaton, T.H., 1990. Evidence for and implications of self-healing pulses of slip in earthquake rupture. Phys. Earth Planet Inter. 64, 1–20.

Hernandez, B., Cotton, F., Campillo, M., 1999. Contribution of Radar interferometry to a two-step inversion of the kinematic process of the 1992 Landers earthquake. J. Geophys. Res. 104, 13,083–13,099.

Krieg, R.O., Key, S.W., 1973. Transient shell response by numerical time integration. Int. J. Numer. Methods. Eng. 7, 273–286.

Li, Z., Bi, X., Lambros, J., Geubelle, P.H., 2002. Dynamic fiber debonding and frictional push-out in model composite systems: experimental observations. Exp. Mech. 42, 417–425.

Lin, A., Guo, J., Zeng, Q., Dang, G., He, W., Zhao, Y., 2002. Co-Seismic strike-slip and rupture length produced by the 2001 Ms 8.1 central Kunlun earthquake. Science 296, 2015–2017.

Linker, M.F., Dieterich, J.H., 1992. Effects of variable normal stress on rock friction: observations and constitutive equations. J. Geophys. Res. 97, 4923–4940.

Lykotrafitis, G., Coker, D., Rosakis, A.J., Needleman, A., 2005, in preparation.

Madariaga, R., Olsen, K.B., 2000. Criticality of rupture dynamics in 3-D. Pure Appl. Geophys. 157, 1981–2001.

Mouwakeh, M., Villechaise, B., Godet, M., 1991. Quantitative study of interface sliding phenomena in a two-body contact. Eur. J. Mech. A/Solids 10, 545–555.

Needleman, A., 1999. An analysis of intersonic crack growth under shear loading. J. Appl. Mech. 66, 847–857.

Nielsen, S., Madariaga, R., 2003. On the self-healing fracture mode. Bull. Seismol. Soc. Am. 93, 2375–2388.

Olsen, K.B., Madariaga, R., Archuleta, R.J., 1997. Three-dimensional dynamic simulation of the 1992 Landers earthquake. Science 278, 834–838.

Peirce, D., Shih, C.F., Needleman, A., 1984. A tangent modulus method for rate dependent solids. Comp. Struct. 18, 875–887.

Perrin, G., Rice, J.R., Zheng, G., 1995. Self-healing slip pulse on a frictional surface. J. Mech. Phys. Solids 43, 1461–1495.

Povirk, G.L., Needleman, A., 1993. Finite element simulations of fiber pull-out. J. Eng. Mater. Tech. 115, 286–291.

Prakash, V., 1998. Frictional response of sliding interfaces subjected to time varying normal pressures. J. Tribol. 120, 97–102.

Prakash, V., Clifton, R.J., 1993. Pressure-shear plate impact measurement of dynamic friction for high speed machining applications. Proceedings of the Seventh International Congress on Experimental Mechanics. Society of Experimental Mechanics, Bethel, CT, pp. 556–564.

Ranjith, K., Rice, J.R., 2001. Slip dynamics at an interface between dissimilar materials. J. Mech. Phys. Solids 49, 341–361.

Renardy, M., 1992. Ill-posedness at the boundary for elastic solids sliding under Coulomb friction. J. Elasticity 27, 281–287.

Rice, J.R., 2001. New perspectives on crack and fault dynamics. In: Aref, H., Philips, J.W. (Eds.), Mechanics for a New Millennium. Kluwer Academic Publishers, Dordrecht, pp. 1–24.

Rice, J.R., Ben-Zion, Y., 1996. Slip complexity in earthquake fault models. Proc. Natl. Acad. Sci. USA 93, 3811–3818.

Rice, J.R., Ruina, A.L., 1983. Stability of frictional sliding. J. Appl. Mech. 50, 343–349.

Rice, J.R., Lapusta, N., Ranjith, K., 2001. Rate- and state-dependent friction and the stability of sliding between elastically deformable solids. J. Mech. Phys. Solids 49, 1865–1898.

Rosakis, A.J., 2002. Intersonic shear cracks and fault ruptures. Adv. Phys. 51 (4), 1189–1257.

Rosakis, A.J., Samudrala, O., Coker, D., 1999. Cracks faster than the shear wave speed. Science 284, 1337–1340.

Rosakis, A.J., Samudrala, O., Coker, D., 2000. Intersonic shear crack growth along weak planes. Mater. Res. Innov. 3, 236–243.

Rubio, M.A., Galeano, J., 1994. Stick-slip dynamics in the relaxation of stresses in a continuous elastic medium. Phys. Rev. E 50, 1000–1004.

Ruina, A.L., 1983. Slip instability and state variable friction laws. J. Geophys. Res. 88, 10,359–10,370.

Samudrala, O., Huang Y., Rosakis, A.J., 2002. Subsonic and intersonic shear rupture of weak planes with a velocity weakening cohesive zone. J. Geophys. Res. 107, B8 article no. 2170.

Schallamach, A., 1971. How does rubber slide? Wear 17, 301–312.

Tsai, K.-H., Kim, K.-S., 1996. The micromechanics of fiber pull-out. J. Mech. Phys. Solids 44, 1147–1177.

Tullis, T.E., 1996. Rock friction and its implications for earthquake prediction examined via models of Parkfield earthquakes. Proc. Natl. Acad. Sci. 93, 3803–3810.

Xia, K., Rosakis, A.J., Kanamori, H., 2004. Laboratory earthquakes: the sub-Rayleigh-to-supershear rupture transition. Science 303, 1859–1861.

Zheng, G., Rice, J.R., 1998. Conditions under which velocity-weakening friction allows a self-healing versus a crack-like mode of rupture. Bull. Seismol. Soc. Am. 88, 1466–1483.